The protocataclasite dilemma: *in situ* [36]Cl and REE-Y lessons from an impure limestone fault scarp at Sparta, Greece

Bradley W. Goodfellow[1,2,3,4], Marc W. Caffee[5,6], Greg Chmiel[5], Ruben Fritzon[1,3#], Alasdair Skelton[2,3], Arjen P. Stroeven[1,3*]

[1]Department of Physical Geography, Stockholm University, Stockholm, Sweden
[2]Department of Geological Sciences, Stockholm University, Stockholm, Sweden
[3]Bolin Centre for Climate Research, Stockholm University, Stockholm, Sweden
[4]Geological Survey of Sweden, Killiansgatan 10, Lund, Sweden
[5]Department of Physics and Astronomy/Purdue Rare Isotope Measurement Laboratory, Purdue University, West Lafayette, USA
[6]Department of Earth, Atmospheric, and Planetary Sciences, Purdue University, West Lafayette, USA

*Corresponding author
Email: arjen.stroeven@natgeo.su.se
Phone: +46(0)8-16 4230
#Now at Celsiusskolan, Sporthallsvägen 7, 828 33 Edsbyn, Sweden

Abstract

Reconstructions of paleoseismicity are useful for understanding, and mitigating, seismic hazard risks. We apply cosmogenic [36]Cl exposure-age dating and concentrations of rare-earth elements and yttrium (REE-Y) to the paleoseismic history of the Sparta fault, Greece. Bayesian-inference Markov chain Monte Carlo modeling of [36]Cl concentrations along a 7.2 m-long vertical profile on the Sparta Fault scarp at Anogia indicate an increase in average slip rate of the scarp from 0.8–0.9 mm yr^{-1} at 6.5–7.7 kyr ago to 1.1–1.2 mm yr^{-1} up to the devastating 464 B.C.E. earthquake. Average exhumation of the entire scarp up to the present day is 0.7– 0.8 mm yr^{-1}. Modelling does not indicate additional recent exhumation of the Sparta fault after 464 B.C.E. The Sparta fault scarp is composed of fault breccia, containing quartz and clay-lined pores, in addition to host rock-derived clasts of calcite and microcrystalline calcite cement. The impurities control the distribution of REE-Y in the fault scarp and contribute spatial variation to [36]Cl concentrations, which precludes the identification of individual earthquakes that have exhumed the Sparta fault scarp from either of these data sets. REE-Y may illustrate processes that localize slip to a discrete fault plane in

37   the Earth's near-surface but their potential use in paleoseismicity would benefit from further

38   evaluation.

40   **Keywords**

41   [36]Cl exposure dating; earthquake; limestone; normal fault; REE-Y; Sparta fault

43   **1 Introduction**

44   Seismic hazard risks are significant in many parts of the world and studying the magnitude,

45   recurrence, mechanisms, and impacts of past earthquakes helps form a basis for mitigating

46   current and future risk. While historical earthquake records are a crucial archive (Gürpinar,

47   2005), their spatial distribution is patchy and the recurrence interval of large earthquakes on

48   many faults predates historical records. Geologic-based inferences regarding earthquake

49   timing, recurrence intervals, and the magnitudes of slip and shaking intensity, are an essential

50   component of seismic hazard risk mitigation (McCalpin, 2009, p. 24). Topographic

51   expressions of tectonic faults, the displacement of surficial sediments revealed in trenches,

52   and geochemical alterations on subaerially exposed fault surfaces, may each provide evidence

53   useful to the study of paleoseismicity (e.g., Benedetti et al., 2002; Dramis and Blumetti,

54   2005; Michetti et al., 2005; Carcaillet et al., 2008; Manighetti et al., 2010; Mouslopoulou et

55   al., 2011; Smith et al., 2014; Cowie et al., 2017; Mozafari et al., 2022). Here we apply

56   concentrations of cosmic-ray-produced (cosmogenic) [36]Cl and rare-earth elements and

57   yttrium (REE-Y) to study paleoseismicity on the Sparta fault at Anogia, Greece (Fig. 1a, b).

58

59   The Mediterranean is a densely populated seismically active region subjected to 7360

60   earthquakes of magnitude *(M)* > 4 during 1998–2010 (Godey et al., 2013). Within the Aegean

61   tectonic plate (Fig. 1a), and around its margins, there were >1450 earthquakes during this

62 period, 77 of which were $M > 5$. In central Greece, earthquakes are associated with normal

63 faults, which occur because of extension of the Aegean plate (Jolivet et al., 2013). In

64 limestone, they may be identified by spectacular scarps, which form from the accumulation

65 of bedrock slip that occurs during successive earthquakes. Holocene fault scarps can be well-

66 preserved (Armijo et al., 1991), making them suitable targets for paleoseismic studies.

67

68 The concentration of cosmogenic ^{36}Cl (Zreda and Noller, 1998; Mitchell et al., 2001;

69 Benedetti et al., 2002; Palumbo et al., 2004; Schlagenhauf et al., 2010; Tesson et al., 2016;

70 Cowie et al., 2017; Iezzi et al., 2021; Mozafari et al., 2022) has been used to infer

71 paleoseismic activity in limestone normal faults. This nuclide is produced from spallogenic

72 and muonic reactions occurring in ^{40}Ca. Following an earthquake, the newly exposed scarp

73 segment accumulates ^{36}Cl, the concentration of which is dependent upon the duration of

74 subaerial exposure, potentially allowing the earthquake to be dated. However, because

75 earthquakes may be closely clustered in time (Bubeck et al., 2015) and the measured ^{36}Cl

76 concentrations may be consistent with a range of models (Goodall et al., 2021), a unique

77 unequivocal fit to a single model may not be possible. Accurately identifying individual

78 earthquakes is further challenged by ^{36}Cl concentrations along vertical profiles that deviate

79 from the theoretically predicted patterns. These deviations appear to be a ubiquitous feature

80 of normal faults developed in limestone (e.g., Benedetti et al., 2002; Palumbo et al., 2004;

81 Tesson et al., 2016; Cowie et al., 2017; Goodall et al., 2021; Mozafari et al., 2022; Dawood et

82 al., 2024). Collectively, these challenges have driven the development of more sophisticated

83 models for ^{36}Cl concentration profiles; for example Bayesian modeling incorporates prior

84 geologic information (Cowie et al., 2017; Beck et al., 2018; Tesson and Benedetti, 2019;

85 Tikhomirov et al., 2019; Goodall et al., 2021, Iezzi et al., 2021) with the goal of making more

86 robust inferences about past tectonic activity.

87

88   Fault scarps may be exhumed by earthquakes clustered within several thousands of years and

89   then lie dormant for similar, or even longer, periods (Wallace, 1987; Friedrich et al., 2003;

90   Benedetti et al., 2013, Cowie et al., 2017). Although this complicates the determination of

91   earthquake recurrence intervals, earthquake clusters followed by intervening quiescence may

92   may be discerned from fault scarp ^{36}Cl concentrations (Goodall et al., 2021). Exposure ages

93   from Holocene faults may provide information essential to determining the seismogenic

94   potential of a fault (Tesson et al., 2016).

95

96   Measurements of REE-Y have also been used to unravel paleoseismic information on

97   limestone fault scarps, frequently together with ^{36}Cl dating (Carcaillet et al., 2008; Manighetti

98   et al., 2010; Mouslopoulou et al., 2011; Tesson et al., 2016; Bello et al., 2023; Moraetis et al.,

99   2023). The distribution of REE-Y vertically along fault scarps may result from exchanges

100   with former hanging-wall soil REE-Y before uplift. REE-Y would be leached from

101   subaerially exposed scarp surfaces through calcite dissolution and accumulate in the surfaces

102   of the hanging wall soil where they form organic complexes (Carcaillet et al., 2008; Bello et

103   al., 2023; Moraetis et al., 2023). Because of low pH, calcite dissolution is highest where the

104   soil surface abuts the scarp and the REE-Y becomes locally enriched in the adjacent scarp

105   surface through soil-to-scarp REE-Y exchange during reprecipitation of calcite. Peaks in

106   REE-Y on fault scarp surfaces that are now subareally exposed may therefore represent

107   former soil surfaces, which are now exposed to leaching and subsequent accumulation in the

108   hanging wall soil, thus completing a cycle. The spacing of these REE-Y peaks may permit

109   identification of the number of slip events and the vertical displacement lengths. These

110   inferences can be made independently of ^{36}Cl measurements. Using both techniques could

111   provide robust paleoseismic information for seismic risk assessment models.

113   The pioneering cosmogenic ^{36}Cl study of the Sparta fault by Benedetti et al. (2002) motivated

114   our studies. Benedetti et al. found evidence at Parori (Fig. 1b) for the historically recorded

115   464 B.C.E. earthquake that destroyed Sparta (Armijo et al., 1991) and five older earthquakes.

116   Interestingly, they were unable to substantiate a displacement from the historical 464 B.C.E.

117   earthquake at nearby Anogia. Our study objectives were to: (i) study slip rates on the Sparta

118   fault at Anogia, by taking advantage of recent advances in both the measurement of ^{36}Cl and

119   earthquake modelling, accounting for all ^{36}Cl production pathways and shielding effects

120   (Schlagenhauf et al., 2010), and Bayesian modelling using prior knowledge such as the 464

121   B.C.E. earthquake (Goodall et al., 2021); (ii) Complement the ^{36}Cl exposure dating with

122   measurements of REE-Y to best constrain the paleoseismic history of this fault.

123

124   **2 Geological Setting**

125   The Sparta fault is a 64 km long, NNW–SSE striking, range-bounding normal fault in

126   southern Peloponnese (Fig. 1a, b). It separates the eastern flank of the Taygetos Mountains

127   (maximum elevation of 2407 m a.s.l.) from the Sparta Basin (Fig. 1b). The Sparta fault is part

128   of a larger normal fault system, which exceeds 150 km in length, and is matched on the

129   western margin of the Taygetos Mountains by the antithetical Kalamata fault and other

130   similar faults located offshore of the Mani Peninsula (Fig. 1a; Armijo et al., 1991). The

131   subaerially exposed scarp of the Sparta fault is developed in late Senonian-Eocene limestones

132   of the Ionian unit (Institute for Geology and Subsurface Research, 1969; Armijo et al., 1991).

133   Folded and tilted Permian to early Triassic pelitic and psammitic sedimentary and

134   metasedimentary units outcrop in the Taygetos Mountains and are also offset by the Sparta

135   fault at depth (Institute for Geology and Subsurface Research, 1969; Armijo et al., 1991).

136   Geomorphic evidence for Quaternary uplift along the eastern flank of the Taygetos

137 Mountains includes steep triangular facets (20°–40°) that are hundreds of meters high along

138 the central portion of the range and decrease in height towards the N and S, wineglass

139 canyons, perched valleys, and alluvial fans having up to 4 m of entrenchment near the Sparta

140 fault trace (Armijo et al., 1991; Benedetti et al., 2002; Pope and Wilkinson, 2005;

141 Papanikolaou et al., 2013). Collectively, the evidence indicates an environment that has been

142 tectonically active during the Holocene.

143

144 The Sparta fault scarp is nearly continuous along strike and it reaches a maximum height of

145 10–12 m in its central portion but tapers towards both ends. Hanging wall erosion associated

146 with stream incision can locally form higher scarp segments. The scarp has a 61–64° dip and,

147 in all but a few locations, slickensides have been eroded away following exhumation. The

148 slope of the hanging wall ground surface matches that upslope of the footwall, which

149 indicates a contiguous hillslope prior to formation of the present scarp and that sediment

150 accumulation at the scarp base is generally minor. Some wedges of sediment are locally

151 present on the hanging wall and in some places are welded to the scarp face, in positions now

152 perched above the hanging wall (Fig. S1). These wedges may have been perched by

153 earthquake-induced displacement on the Sparta fault or are debris deposits from mass

154 movements that have partly eroded. It is possible that other sediment wedges were also

155 formerly attached to the scarp face but have since fallen off.

156

157 Our sampling site is located at Anogia, where the Sparta fault scarp is 6.8 m high (Fig. 1c),

158 sparsely fractured, and displays a smooth surface texture (Fig. 1d-e). Apparent slickensides

159 are faintly visible as grooves that may have been widened and deepened by weathering, and

160 the surface displays a black coating, like those commonly occurring on limestone and which

161 contain higher concentrations of SiO_2 and Al_2O_3 than the underlying rock (Carcaillet et al.,

162   2008). The scarp surface at Anogia also displays a spatially variable distribution of subaerial

163   weathering features such as rills and dissolution pits, which we avoided in our sampling. The

164   lower-angle hillslopes on both the foot wall (above the fault scarp) and hanging wall display

165   a patchy distribution of bedrock outcrops and an indurated allochthonous regolith composed

166   of limestone clasts, with a matrix of red aeolian dust and calcite cement. An outcrop of

167   limestone about 50 m upslope of the fault scarp reveals folded and tilted bedding. The

168   bedding nearest to the scarp has a dip of 45–60° and a strike of 268–279°, which corresponds

169   with those for the fault scarp, indicating that faulting appears to exploit these structural

170   weaknesses in the bedrock. We neither observed scarps with a total offset of 2–3 m within

171   tens of meters downslope of the Sparta fault scarp (Benedetti et al., 2002), nor observed fault

172   scarps within hundreds of meters upslope of the Sparta fault scarp. If earthquakes, including

173   at 464 B.C.E., bypassed the fault scarp at Anogia (Benedetti et al., 2002), they did not leave

174   geomorphic expressions that we observed on field reconnaissance.

175

176

177   **3 Methods**

178   To study the paleoseismicity of the Sparta fault, we combined Accelerated Mass

179   Spectrometry (AMS) measurements of cosmogenic ^{36}Cl concentrations from samples

180   collected from the Sparta fault scarp with field and laboratory analyses of scarp composition

181   and mineralogy, and with field measurements of hanging wall soil composition and pH. We

182   made these measurements by sampling a vertical ^{36}Cl profile at Anogia, upwards from the

183   ground surface and adjacent to the sampling transect of Benedetti et al. (2002) for direct

184   comparison with that pre-existing record (Fig. 1c). We also took samples for ^{36}Cl and

185   mineralogical analyses, including REE-Y, from a second vertical profile located about 50 m

186   to the south (Fig. 1c). We chose this additional site for its smooth, non-fractured, fault scarp

187 surface, and sampling was completed from the top of the scarp to 80 cm below the present

188 ground surface, following hand excavation of a pit.

189

190 **3.1 ^{36}Cl concentrations**

191 We sampled the first profile (Anogia A), adjacent to the southern margin of the Benedetti et

192 al. (2002) profile, for ^{36}Cl by using an angle grinder to cut 10*20*3 cm (*h*w*d*) slabs from

193 the ground surface to a height of 3.9 m (Fig. 1c, d). Because of a crack in the fault scarp at

194 1.1 m above the ground, the transect was shifted laterally (towards the north) by 40 cm, thus

195 duplicating the measurement at 1.1 m. A total of 37 samples from this profile were measured

196 for ^{36}Cl concentration. We sampled the second profile (Anogia B), ~ 50 m further to the

197 south, for ^{36}Cl and mineralogical analyses initially by drilling 14 cores of 4 cm diameter to a

198 depth of 3 cm into the scarp surface (Fig. 1c, e). Four of these cores were spaced at 20 cm

199 intervals below the ground surface and eight were spaced at 80 cm intervals above the ground

200 surface to a height of 6.4 m, which is 0.4 m below the top of the scarp. These samples were

201 augmented by another two drill core samples at 1.2 m and at 6.0 m. Subsequently, we took 20

202 samples from this profile using an angle grinder to cut 10*20*3 cm (*h*w*d*) slabs from the

203 ground surface to a height of 2.0 m (Fig. 1c). A total of 71 samples from the three profiles

204 were subjected to preparation chemistry for ^{36}Cl targets and measured using AMS.

205

206 For ^{36}Cl measurements, limestone samples were crushed to approximately 0.5 mm diameter

207 and the whole sample was used without removing any size fraction through sieving. Prior to

208 partial dissolution approximately 120 g of crushed material was washed with deionized water

209 to remove fines. Following Stone et al. (1996), meteoric ^{36}Cl was removed using two cycles

210 of partial dissolution with nitric acid to dissolve 5% (by mass) of the carbonate each time. To

211 prepare the AMS target we used 30 g of dried sample, spiked with 1 mg of ^{35}Cl-enriched

sodium chloride carrier (Source: Icon Isotopes, ^{35}Cl 99.635 atom %, ^{35}Cl/^{37}Cl = 273) to

measure native chloride by isotope dilution. A slurry of the sample and 120 g of deionized

water was slowly dissolved with 60 g of concentrated trace-metal grade nitric acid. Post-

dissolution, both liquid and undissolved solids were quantitatively transferred to a centrifuge

bottle where the solids were removed by centrifugation. The supernatant was decanted to

another centrifuge bottle and chloride was precipitated using one molar silver nitrate. After a

settling period, the bottle was centrifuged to isolate the silver chloride which was then

washed, dissolved with ammonium hydroxide, and treated with barium nitrate to remove

sulfate in preparation for further purification by chromatography. The solution was loaded

onto 5 ml of Bio-Rad AG 1-X8 strong anion-exchange resin and chloride was moved through

with 0.50 mmol, and then 0.150 mmol, nitric acid. After re-precipitation with silver nitrate

and a washing step the silver chloride was dried and packed into silver bromide-cored copper

holders. AMS measurements were performed at the Purdue Rare Isotope Measurement

Laboratory according to procedures in Muzikar et al. (2003); standards used for the

measurement are described in Sharma et al. (1990).

3.1.1 Bayesian modelling of ^{36}Cl concentrations

We apply the Bayesian Markov chain Monte Carlo (MCMC) code from Goodall et al. (2021)

to identify slip rates from ^{36}Cl concentrations. MCMC builds upon 'modelscarp' from

Schlagenhauf et al. (2010), which models the number of earthquakes, their ages, and resulting

displacements from ^{36}Cl concentrations based on user-defined inputs. 'Modelscarp' accounts

for each ^{36}Cl production pathway in limestone (Table 1 in Schlagenhauf et al., 2010). The

Goodall et al. (2021) MCMC code is adapted from Cowie et al. (2017) to generate potential

slip histories.

The MCMC code models: (i) scarp age, which is the timing of the earthquake to exhume the uppermost, and therefore oldest, part of the fault scarp; (ii) time at which each subsequent earthquake occurred and the corresponding height of exhumed scarp, and; (iii) time since the most recent earthquake exhumed the lowest part of the fault scarp (elapsed time). The exhumation of the entire scarp is attributed to a user-defined number of earthquakes that each exhumed the same vertical length of scarp. The timing of each earthquake, apart from the first and last, is dependent on the selected number of earthquakes. We follow Goodall et al. (2021) in using the flexible change point method of Cowie et al. (2017), which allows for variable slip rates between iterations.

We parametrized the MCMC model as follows. (i) We defined the scarp age as 8000 years with a 1σ normally distributed prior of 1500 years. This selection is partly based on the record that contemporary faults scarps in the Mediterranean region are Holocene in age. They have been exhumed since the last glacial maximum (LGM) because hillslope bedrock erosion and regolith transport rates were much higher during the LGM (e.g., more than ten times higher for the Magnola Fault in Italy; Tucker et al., 2011), preventing ruptured fault scarps from persisting as subaerially exposed features (e.g., Benedetti et al., 2002; Cowie et al., 2017; Goodall et al., 2021). The adopted scarp age is refined as a consequence of fitting a modelled ^{36}Cl concentration profile to the measured ^{36}Cl concentration profile using the 'modelscarp' code of MCMC. The scarp age is also balanced by the period of pre-exposure, which is the ^{36}Cl inventory that accumulated in the bedrock while it was mantled by a up to a few meters of colluvium before initial post-LGM subaerial exposure. A wide Gaussian prior (5000–16 000 years), is assigned in our modeling to account for the uncertainty in scarp age. (ii) The elapsed time is defined as 2500 years, based on the youngest known earthquake on the Sparta Fault of 464 B.C.E. We assign a 1σ uncertainty of 1000 years to reflect uncertainty

262   in the historical record. (iii) To further define the most likely slip rate history for the Sparta

263   fault, we completed multiple model runs with varying number of earthquakes (three to six)

264   and ^{36}Cl spallation production rates (48.8 ± 3.5 to 59.4 ± 4.3 atoms g Ca^{-1} yr^{-1}). These end-

265   member production rates are from Stone et al. (1996) and Schlagenhauf et al. (2010)

266   calculated from Lifton et al., (2005), respectively. All model runs used the temporally

267   variable geomagnetic field of Lifton et al. (2005) to scale the ^{36}Cl spallation production rate

268   and spallation production rates for K, Ti, and Fe are as shown in Table 1 from Schlagenhauf

269   et al. (2010). Scarp age and elapsed time are the priors in the MCMC model, the number of

270   earthquakes defines the timing and location on the scarp of slip change points, and prior

271   probabilities are as defined in the Goodall et al. (2021) MCMC code.

272

273   The MCMC algorithm generates a slip history, using the input parameters conditioned on

274   prior probability, to construct a forward model of ^{36}Cl concentrations for this slip history

275   (Goodall et al., 2021). The quality of the slip history solution is then assessed by comparing

276   modelled and measured ^{36}Cl concentration profiles. The algorithm iteratively adjusts a

277   parameter defining the slip history and recalculates a new forward model solution.

278   Acceptance of the new slip history hinges on either its likelihood surpassing that of the prior

279   model or the ratio of new to current likelihood exceeding a randomly selected value from a

280   uniform distribution between zero and one. Otherwise, the new model solution is discarded,

281   adhering to the principles of the Metropolis-Hastings algorithm (Metropolis et al., 1953;

282   Hastings, 1970). We ran this process for 200 000 iterations, using the parameters in Table 1,

283   and results were assessed on 160 000 iterations after a burn-in phase of 40 000 iterations were

284   excluded to mitigate the influence of initial parameters.

285

286   **3.2 Sparta fault scarp composition**

287 Fault scarp chemical composition and mineralogy were analyzed from Anogia B as follows.

288 An initial elemental analysis was done in the field on the Sparta fault scarp surface using an

289 Olympus Innov-X Delta (40 kV) handheld X-ray fluorescence (XRF) device. This instrument

290 performs elemental analyses with a circular sample spot of 8 mm diameter and can measure

291 elements heavier than Na. All elements lighter than Mg are reported as lighter elements (LE).

292 Of the elements that compose REE-Y, it was only capable of measuring yttrium. Sampling

293 was done at an interval of 5 cm (or less) over a 7.7 m vertical profile, beginning ~0.9 m

294 below the hanging wall soil surface. This profile corresponds with the location of the drill

295 core and 2.0 m-long ^{36}Cl profiles at Anogia B but was measured before either drilling or slab

296 sampling (Fig. 1c).

297

298 For more detailed analyses of elements, including REE-Y, a total of 39 cores (22 mm and 35

299 mm diameters and to depths of ~3 cm) were collected every 20 cm from a vertical transect at

300 Anogia B using a portable drill (Fig. 1d). The outermost 1 mm was removed from each core

301 prior to crushing to avoid contamination from the black surface coating. The next 15 mm of

302 each core were then rinsed with cold water, air dried, and crushed using a grinder with a steel

303 mortar to a grain size of <100 μm. This crushing technique might supply additional REE-Y to

304 samples (Hickson and Juras, 1986) but if so, this likely occurs systematically across samples

305 and we are more interested in spatial trends, which we confirm independently using the

306 handheld XRF, than absolute abundances. The crushed samples were then analyzed for major

307 and trace elements using fusion inductively coupled plasma mass spectrometry (FUS-ICP-

308 MS) at Activation Laboratories (Ontario, Canada).

309

310 We complemented the FUS-ICP-MS analyses with spot elemental analysis of one rock core

311 from 1.1 m above the scarp base at Anogia B to make a high-resolution determination of any

312 spatial variations in the scarp composition. This was done with an energy-dispersive X-ray

313 spectroscope (EDS) attached to an environmental scanning electron microscope (ESEM). We

314 used a Quanta FEG 650 with Oxford-Inka EDS, and the analysis was made in a high-vacuum

315 environment at 20 kV. The technique is incapable of detecting REE-Y because their

316 concentrations are too low. Photomicrographs and backscatter images of pore spaces were

317 also taken using the ESEM. These analyses were completed at the Department of Geological

318 Sciences, Stockholm University.

319

320 **3.3 Sparta fault scarp mineralogy**

321 A modal analysis of mineral fractions was completed on thin sections taken from the

322 remaining 38 core samples. This was done by counting 1000 points on each thin section

323 (Hutchison, 1974) using a Pelcon automatic point counter attached to a Leica (DM LSP)

324 optical microscope. This point counter comprises a stepping frame attached to a control box

325 (power supply) and is also connected to a computer for statistical analyses using Pelcon

326 software version 2. The point counting and mineral identification was made using an

327 objective working distance of 1.52 mm. The line section pre-set step-length was 0.3 mm and

328 the line section distance was 1.5–2 mm. The point counting permitted a detailed quantitative

329 analysis of the mineralogy of the Sparta fault scarp surface. This detailed mineralogy was

330 then compared with the chemical composition data to determine whether phases other than

331 the host limestone are present.

332

333 **3.4 Hanging wall soil chemistry and pH**

334 Soil chemistry and pH were measured in samples taken at ~10 cm intervals to a depth of ~90

335 cm in the pit excavated at the base of the Anogia B profile (Fig. 1c). The elemental analysis

336 was again done with the handheld XRF device. Indicator strips were used to measure pH

337   from mixtures of 1:1 mass ratio of soil:distilled water, and soil:1 M KCl (Sikora and Moore,

338   2014). These analyses help determine the vertical distribution of REE-Y in the soil (using

339   yttrium as a proxy) and indicate how they might correlate with pH and the vertical

340   distribution of REE-Y in the fault scarp below the soil surface.

341

342   **4 Results**

343   **4.1 Sparta fault ^{36}Cl concentrations**

344   The cosmogenic nuclide ^{36}Cl concentrations from our three profiles (Table S1) and the

345   original Benedetti et al. (2002) ^{36}Cl concentrations are compared in Figure 2. The Anogia A

346   and Anogia B profiles display corresponding trends of increasing ^{36}Cl concentrations with

347   increasing height on the fault scarp. Only at 1.6 m do the trends strongly deviate from each

348   other. The Anogia B profile indicates generally lower ^{36}Cl concentrations including six of 19

349   points that do not overlap within uncertainty with data points at corresponding elevations on

350   the Anogia A profile. Four of those points are located from 1.0 m to 1.3 m. In comparison

351   with Anogia A, the adjacent segment of the Benedetti et al. (2002) profile (0–4 m) shows ^{36}Cl

352   concentrations that are on average 19% higher. Uncertainties (1σ) for data points comprising

353   each profile are almost identical, displaying a mean of 3.8% for the Benedetti et al. (2002)

354   profile versus 3.9% for the Anogia A and Anogia B profiles. However, the Benedetti et al.

355   (2002) profile displays more variation between adjacent sample points than is evident in our

356   profiles. Whereas concentrations differ between the three longest profiles, they show a

357   consistent gradient up to ~4 m on the scarp. Above 4 m on the scarp, both our Anogia B drill-

358   core profile and the Benedetti et al. (2002) profile display matching lower gradients. Whereas

359   differences in measured concentrations between our two profiles and the Benedetti et al.

360   (2002) profile might be expected given technical advances between measurements,

361   successive samples in our data display inconsistent variations between the Anogia A and B

362   profiles, despite them being horizontally separated by only ~ 50 m. This inability to replicate

363   measurements along two adjacent profiles justifies a focus on identifying slip rates using the

364   Goodall et al. (2021) model, rather than individual earthquakes, also because up-scarp ^{36}Cl

365   concentration gradients are more consistent between the profiles.

366

367   Slips rates for the Sparta fault are explored through comparing scarp exhumation generated

368   by three, five, and six modelled earthquakes, where each earthquake exhumes 183 cm, 122

369   cm, and 104 cm, respectively. We focus our analyses on the Anogia A profile supplemented

370   with drill core samples from above 3.9 m on the scarp and from the scarp surface buried by

371   colluvium. This combined profile was chosen for modelling both because the Anogia A

372   profile was sampled at 10 cm intervals up to 3.9 m on the scarp, versus only 2.1 m for Anogia

373   B, and because Anogia A is located adjacent to the Benedetti et al. 2002 profile. Furthermore,

374   MCMC modelling of ^{36}Cl concentrations did not converge with measured concentrations for

375   the full Anogia B profile (i.e., including the drill core samples above 2.1 m), but rather only

376   for the intensively sampled lowermost 2.1 m plus subsurface drill core samples. Modelling

377   only the lowermost 2.1 m plus subsurface drill core samples necessitated changes to scarp

378   age and preexposure from those used for the Anogia A plus drill core sample profile, because

379   this lowermost part of the scarp has a younger age, and to slip length because the 2.1m profile

380   length is indivisible into the 6.5 m length of the Anogia A plus drill core sample profile.

381   These changes, especially to scarp age, invalidate comparisons of slip rates between the two

382   profiles, which are the focus of this paper. We did not measure compositions for the Anogia

383   A samples, so we use a mean scarp composition from Anogia B in our modelling. Results

384   from the Goodall et al. (2001) model applied to the Anogia A plus drill core profile are

385   shown below and in Figure S2, respectively, for end-member ^{36}Cl productions rates of 59.4 $\pm$

386   4.3 atoms g Ca^{-1} yr^{-1} from Schlagenhauf et al. (2010) calculated from Lifton et al., (2005) and

387   48.8 ± 3.5 atoms g Ca^{-1} yr^{-1} from Stone et al. (1996). Geochemical data for the fault scrap

388   used in modelling are shown in Table S2. Modelling results from Anogia B (lowermost 2.1 m

389   and subsurface drill core samples and the entire profile) are shown in Figure S3.

390

391   The results of the Bayesian inference MCMC modelling of ^{36}Cl data from the Sparta fault are

392   shown in Figures 3–5. The accepted scarp exhumation models (n = 160 000) are shown in

393   slip versus time histograms (Fig. 3a). The maximum a posteriori probability (MAP) model,

394   shown by the red line, deviates slightly from the maximum model density (mean model,

395   black line) for each slip segment, but more so for the slip segment at 4.9–6.1 m on the scarp.

396   It indicates three exhumation events between 2.4 and 6.1 m on the scarp, that are closely

397   spaced in time at 5000-6000 years ago. The 95% confidence intervals (Fig. 3b) illustrate little

398   change in variance between model results from lower, younger parts of the scarp to older,

399   higher parts of the scarp, although the MAP model deviates towards being younger than the

400   mean model towards the top of the scarp. The range of accepted models fits the measured

401   ^{36}Cl data well (Fig. 3c) but accommodates a broad range of corresponding slip histories along

402   the entire vertical length of the scarp (Fig. 3d).

403

404   Statistics for how well the MCMC modelling fits the measured ^{36}Cl data and our initial

405   estimates of scarp age (8000 years) and elapsed time (2500 years) are illustrated in Figure 4

406   and summarized in Table S2. The posterior probability distribution function indicates that the

407   elapsed time since the most recent earthquake is consistent with the 464 B.C.E. earthquake

408   (mean of 2501 ± 164 years; Fig. 4a). In contrast, the time when the scarp started to form

409   (scarp age), presumably through a decrease in hillslope erosion following the LGM, is

410   indicted by the posterior probability distribution to have been longer than our initial estimate

411   of 8000 years (mean of 8742 ± 502 years; Fig. 4b). Mean values of likelihood, weighted

412 mean root square (RMS$_w$) and corrected Akaike's Information Criterion (AICc) are 0.25–

413 0.28, 13.9–14.6, and 863–893, respectively, across the modelled range of the number of slip

414 events (Figs. 4d and 4e; Table S2), indicating that the number of earthquakes (change points)

415 has minor influence on modelling a fit to measured ^{36}Cl concentrations.

416

417 The slip rate for the Sparta Fault is calculated from the most probable of models (i.e., the top

418 6.25% of fits to the ^{36}Cl data (n = 10 000); Fig. 5, Table 2). For the entire vertical length of

419 the fault scarp, and five modelled earthquakes, both the mean and MAP slip rates are 0.7–0.8

420 mm yr^{-1} for end-member ^{36}Cl production rates, calculated up to the present day (Fig. 5a). For

421 the same calculation but excluding the 2500 year since the most recent known earthquake at

422 464 B.C.E., the slip rates are higher, with mean and MAP values of 1.1 and 1.2 mm yr^{-1},

423 respectively (Fig. 5b). The lowest 3.7 m of the fault scarp is the most recently exhumed scarp

424 segment and the most intensively sampled. It displays a steep ^{36}Cl concentration gradient,

425 which indicates matching mean and MAP slip rates of 1.0 mm yr^{-1}, for five model

426 earthquakes (Fig. 5c). The highest 2.5 m of the scarp displays a gentler ^{36}Cl concentration

427 gradient relative to the bottom 3.9 m of the scarp as indicated by our drill core samples and

428 the Benedetti et al. (2002) profile. The mean and MAP slip rates for this scarp segment are

429 therefore lower, at 0.8–0.9 mm yr^{-1} (Fig. 5d). Varying the number of earthquakes between

430 three and six has minor influence on the calculated slip rates (Table 2). An increase in mean

431 slip rate occurred between 6.7 and 5.3 kyr (Fig. 5e).

432

433 **4.2 Granulometry of the Sparta fault scarp surface**

434 A first look at the Sparta fault scarp surface yields a misleading impression of homogeneous

435 limestone (Figs. 1, 6a), whereas close inspection of the core samples instead reveals a typical

436 fault breccia (Figs. 6b-d). This breccia consists of angular-to-rounded limestone clasts with

437   axes of 1–7 mm (in the two-dimensional view provided by thin sections) surrounded by

438   matrix/cement in which clasts are <0.1 mm in length. The fault breccia is defined as a

439   protocataclasite, according to the classification of Woodcock and Mort (2008). The

440   composition of the protocataclasite displays large spatial variations, with some portions

441   containing abundant clasts (Fig. 6c), whereas others are dominated by fine matrix (Fig. 6d).

442   The proportion of clasts >2 mm ranges from 5% to 20% vertically along the fault scarp and

443   the proportion of matrix ranges from 5% to 60%. We did not measure the thickness of the

444   protocataclasite but it everywhere exceeds the 3 cm depth of our drill cores.

445

446   **4.3 Sparta fault scarp composition and mineralogy**

447   In addition to a spatially variable granulometry, the fault scarp shows a spatially variable

448   distribution of major and trace elements. The major component is, as expected for limestone,

449   CaO (mean 52.22%) but its concentration varies between 43.83% and 56.64% (Table S3),

450   which exceeds spatial variations in CaO seen elsewhere in limestone normal fault scarps

451   (Carcaillet et al., 2008; Tesson et al., 2016). Quartz (SiO_2) also occurs, and it too displays

452   spatial variations (0.10%–20.82%), with broad peaks occurring at 0.5–0.4 m below the

453   ground, and 0.9–1.2 m, 4.6–4.8 m, and 6.0–6.2 m along the vertical fault scarp profile (Fig. 7;

454   Table S3). An additional peak in SiO_2, but which is not seen in point counting of quartz,

455   occurs at 6.2 m (Fig. 7; Tables S3 and S4). Mean concentrations of other major elements are

456   low in bulk samples, including Al_2O_3 (0.21%), MgO (0.16%), Fe_2O_3 (0.09%), P_2O_5 (0.07%),

457   and K_2O (0.05%; Table S3). However, EDS measurements, such as shown in Figure 8a,

458   reveal that the concentrations of some elements are frequently much higher in intergranular

459   pores (Fig. 8c) than elsewhere in the fault scarp, including Si ≤ 38.3%, Al ≤ 11.7%, Fe ≤

460   48.4%, and K ≤ 7.1% (Table S5). Furthermore, intergranular pores and quartz frequently

461   occur together (Fig. 8b) and the concentration of Al_2O_3 covaries with the much more

462   abundant quartz (SiO_2) (Fig. 7).

463

464   Quartz is revealed by microscopy to be present as randomly oriented rounded-to-angular

465   grains that are <50 μm in diameter (Figs. 6d, 8b). Quartz is a constituent of the

466   protocataclasite fine matrix that is mostly comprised of microcrystalline calcite precipitates

467   and which cements larger host rock-derived $CaCO_3$ clasts (Figs. 6b-d, 8b, 9a). Point counting

468   further reveals quartz modes ranging from 0.1% to 15.4% of thin section area (Table S4),

469   with higher abundances correlating to higher abundances of fine matrix. The spatial

470   correlations between SiO_2, quartz abundances on point counting, and fine matrix are further

471   strengthened by EDS spot elemental analyses (Fig. 9). Here, the two selected spots in the fine

472   matrix display Si abundances of 29.7% and 28.9%, which contrasts with 1.7% and 0.9% for

473   the two spots located on clasts. CaO abundances display an inverse relationship with SiO_2

474   (33.7% and 31.2% for the clasts versus 4.8% and 5.1% for the fine matrix). SiO_2 is present

475   largely as quartz, as evidenced by the strong spatial correlation between quartz and SiO_2

476   along the vertical profile (Fig. 7). Quartz can therefore be used as a proxy for fine matrix

477   abundances in the Sparta fault scarp.

478

479   In addition to the spatial relationship between quartz and fine matrix, we observed in

480   backscatter SEM images that pore spaces, which frequently harbor higher concentrations of

481   Si, Al, K and/or Fe than host rock-derived clasts, are also more abundant in the fine matrix

482   (Fig. 8c). These observations provide evidence that clay particles (< μm-scale) frequently

483   coat pore spaces. The abundance of quartz therefore also provides a proxy for the abundance

484   of clay-coated pore spaces.

485

486 Concentrations of REE-Y vary in a wave-like pattern along the vertical profile, with maxima

487 occurring at -0.4 m, 0.8 m, 2.6 m, 4.0 m, and 6.4 m (Y = 1.2–11.1 ppm; Table S6; Fig. 10).

488 These maxima do not systematically decrease with vertical distance above the hanging wall

489 and are not highest in the soil-mantled portion of the scarp. Yttrium (mean 6.3 ppm), La

490 (mean 5.04 ppm), Nd (mean 3.54 ppm), and Ce (mean 2.31 ppm) have the highest

491 concentrations, whereas all other REE-Y are <1 ppm (Table S6). The concentrations of REE-

492 Y elements co-vary vertically along the scarp surface (R^2 = 0.95; Fig. 10a).

493

494 There is no depletion of light (LREE) relative to heavy (HREE) rare-earth elements with

495 increasing height on the subaerially exposed fault scarp, where it ranges between 3.9 and 5.1

496 (Figs. 10b, 11a, Table S6). However, there is a relative depletion of LREE on the scarp

497 surface buried by soil (LREE/HREE is 3.2 to 4.0; Figs. 10b, 11a), with least depletion at 0.40

498 m depth and progressively larger LREE depletion with increasing depth. Peaks and troughs in

499 the LREE/HREE ratio along the vertical profile poorly match peaks and troughs in REE-Y

500 concentrations (Figs. 10a, b), although local minima correspond at 3 m and at 5.2 m on the

501 scarp. Accordingly, the correlation between LREE/HREE and total REE-Y concentration is

502 only weak (R^2 = 0.36; Fig. 11b).

503

504 REE-Y concentration maxima occur at locations that correspond closely with the Al_2O_3

505 maxima (Fig. 10a; Table S6). Accordingly, LREE, HREE, and total REE-Y are strongly

506 correlated with Al_2O_3 (R^2 = 0.92; Figs. 11c, S3a). Spatial correlations between REE-Y and

507 SiO_2 and K_2O are also observed (R^2 = 0.56 and 0.87, respectively; Fig. S4c, e). Whereas

508 REE-Y concentrations vary in wave-like pattern along the scarp, REE-Y is not enriched, and

509 LREE is depleted relative to HREE, in the soil-covered scarp surface.

510

4.4 Hanging wall soil chemistry and pH

The terra rosa soil mantling the hanging wall primarily comprises aeolian dust (Muhs et al., 2010) and carbonate clasts. At our sample site, the soil thickness at the base of the Sparta fault scarp is 0.8 m and this appears to be stable, at least over the timescale of scarp surface dissolution, as evidenced by a much smoother scarp surface texture below the soil surface compared with the subaerially exposed scarp. Below the organic horizon (~0.1 m thick) the soil is welded, probably by calcite precipitates, and horizons are absent. Soil pH is, in general, slightly acidic along the excavated vertical profile, remaining within a 6.2 to 7.0 range (Fig. 12a; Table S7). An outlier occurs at -0.30 m, where the pH is 5.6 ± 0.2. Soil composition varies with depth (Fig. 12b; Table S8). Concentrations of Si, Al, and K are lower in the organic horizon (11%, 0–5%, and 0.4%, respectively) compared with the remainder of the profile (18%–30%, 5–10%, and 0.5–0.9%, respectively), whereas the concentrations of LE, which includes C, are, as expected, higher in the organic horizon (75%–80%) than in the lower profile segment (51%–64%). The concentration of yttrium ranges from a maximum of 36–39 ppm at 0.5– 0.6 m depth to a minimum of 11 ppm at 0.1 m depth and its vertical distribution correlates positively with Si ($R^2 = 0.71$), Al ($R^2 = 0.45$), and K ($R^2 = 0.54$), and negatively with pH ($R^2 = -0.52$; Figs. 12c, S4b,d,f; Table S8).

5 Discussion

5.1 Slip rate on the Sparta Fault at Anogia

Average exhumation of the entire scarp up to the present day is 0.7– 0.8 mm yr^{-1} (Fig. 5a; Table 2). This compares with an exhumation rate of 1.1–1.2 mm yr^{-1} up to the 464 B.C.E. earthquake (if an earthquake occurred now, the rate up to the present day would increase). Our data show an increase in average slip rate during exhumation of the scarp from an initial 0.8–0.9 mm yr^{-1} between 6.5 and 7.7 kyr ago to 1.0 mm yr^{-1} between 3.0 and 6.0 kyr ago

536   (Fig. 5e). These slip rates directly reflect the steeper ^{36}Cl gradient for the lower 4.0 m of the

537   fault scarp compared with the gentler gradient from 4.0 to 6.5 m (Figs. 2 and 3c). Although

538   the sampling density is highest over the lowermost 4 m, we have confidence in the lower

539   inferred average slip rate for the higher, older part of the scarp because both our dispersed

540   drill core samples and the Benedetti et al. (2002) profile indicate a lower ^{36}Cl concentration

541   gradient (in trend, rather than absolute values) above 4 m. The MAP model (Fig. 3a) indicates

542   that three scarp exhuming earthquakes may have occurred during 5000-6000 years ago (MAP

543   average slip rate 1.1 mm yr^{-1}), which is consistent with an increase in average slip rate during

544   this period observed in the slip rate versus time plot (Fig. 5e). The lower rate of exhumation

545   for the upper ~2.5 m reflects an apparent quiescent period prior to these earthquakes. MCMC

546   modelling does not indicate that earthquakes have contributed to exhumation of the Sparta

547   fault more recently than the last historically recorded event at 464 B.C.E. Periods of

548   quiescence appear to characterize normal faults in the Mediterranean region (Cowie et al.,

549   2017; Goodall et al., 2021) and so the recent 2.5 kyr period of quiescence is not necessarily

550   indicative that another earthquake is imminent.

551

552   Our data do not uniquely specify the number and timing of scarp exhumation events and we

553   have been unable to identify other faults along the eastern flank of the Taygetos Mountains

554   suitable for ^{36}Cl analyses that with the Sparta fault may form part of a system, across which

555   slip is distributed. We therefore limit our interpretations to averaged slip rates and the timing

556   of changes in these rates for the Sparta fault at Anogia, rather than attempting to identify

557   individual earthquakes or draw conclusions on regional fault kinematics and associated

558   seismic hazards.

559

560   **5.2 Methodological and geological sources of uncertainty in the ^{36}Cl data**

561 A feature of the ^{36}Cl data is that our Anogia A and B profiles display systematically lower

562 concentrations than the Benedetti et al. (2002) profile (Fig. 2). The Benedetti et al. (2002)

563 profile also displays variations between adjacent sample points that exceed those observed in

564 our profiles. We interpret the systematic differences in ^{36}Cl concentration between our

565 profiles and the Benedetti et al. (2002) profile as reflecting methodological differences

566 related to advances in sample preparation chemistry at PRIME-Lab, Purdue University. For

567 this reason, we elect not to model the Benedetti et al. (2002) data using the MCMC

568 methodology.

569

570 Whereas our Anogia A and B profiles display corresponding trends with increasing elevation

571 on the fault scarp, Anogia B samples have generally lower ^{36}Cl concentrations (Fig. 2).

572 Indeed, six of its 19 ^{36}Cl concentrations do not overlap within uncertainty with concentrations

573 of corresponding samples on the 3.9 m Anogia A profile, including four points located

574 between 1.0 m and 1.3 m. We interpret these differences as indicating that the fault scarp at

575 Anogia B has been either partly shielded from cosmogenic radiation, has eroded more than

576 the scarp surface at Anogia A, or contains a higher concentration of non-calcite impurities. Of

577 potential additional relevance is that the texture of the scarp surface at Anogia B is smoother

578 than at the location of Anogia A. Because a similarly smooth texture also characterizes the

579 scarp surface presently buried by colluvium mantling the hanging wall, the smooth texture at

580 the location of Anogia B may indicate either recent burial of the scarp surface by colluvium

581 and/or CaCO$_3$ dissolution/reprecipitation occurring at a higher rate than at locations where

582 the exposed scarp surface texture is rougher. If a smooth texture reflects erosion through

583 CaCO$_3$ dissolution, there might be preferential flow, or seepage, of water from the hillslope

584 above the scarp at the location of Anogia B. Observed lumps of colluvium cemented to the

585 Sparta fault scarp, at locations perched above the present hanging wall surface (Fig. S1)

586 partially shield the underlying scarp surface today. However, had this previously occurred at

587 the location of Anogia B, an eroded colluvial lump would be evidenced in the hanging wall

588 sediments. On the contrary, there is no colluvial lump, but rather a sub-horizontal surface is

589 present with an expression that differs little from the surface below the Anogia A profile. The

590 inter-profile differences in ^{36}Cl concentrations illustrate the value in taking samples for ^{36}Cl

591 measurements from more than one vertical profile at a particular location, because ^{36}Cl

592 concentrations can vary either through spatial variations in non-calcite impurities or past

593 shielding by sediments or bedrock, which can otherwise be difficult to detect. Partial

594 shielding may impact the interpretation of paleoseismicity, including the timing, number and

595 magnitudes of earthquakes, through locally lowered ^{36}Cl concentrations.

596

597 **5.3 The effects of mineralogical impurities on ^{36}Cl concentrations**

598 Mineralogical impurities embedded in the fault breccia that comprise the scarp surface appear

599 to be a key geological reason for spatial variations in the concentration of ^{36}Cl. Measurements

600 of chemistry and mineralogy at Anogia B indicate that SiO_2 comprises 0.1–20.8 wt.% of the

601 scarp. Because the concentration of $CaCO_3$ is inversely correlated with SiO_2 (largely quartz),

602 then peaks in SiO_2 might coincide with troughs in ^{36}Cl, although a simple relationship

603 vertically along the scarp is obscured by the relationship between ^{36}Cl concentration and

604 exposure duration. A local peak in SiO_2 of 12–15 wt.% coincides with a local low in ^{36}Cl

605 concentration at Anogia B between about 0.6 and 1.2 m on the scarp (Figs. 2 and 7, Tables S1

606 and S3). A distinct low in ^{36}Cl concentration at 1.6 m also corresponds with a local peak in

607 SiO_2 of 9 wt.%. However, the magnitudes of the variations are inconsistent between these

608 two locations, such that a high peak in SiO_2 corresponds with a small reduction of ^{36}Cl at

609 0.6–1.2 m and vice versa at 1.6 m. Because ^{36}Cl is also produced by spallation on K (162 $\pm$

610 24 atoms g^{-1} yr^{-1} at SLHL; Evans et al., 1997), Fe (1.3 $\pm$ 0.1 atoms g^{-1} yr^{-1}–1.9 $\pm$ 0.2 atoms g^{-}

611 ^{1} yr^{-1} at SLHL; Stone, 2005; Moore and Granger, 2019), and Ti (13 $\pm$ 3 atoms g^{-1} yr^{-1} at

612   SLHL; Fink et al., 2000), noise in the ^{36}Cl data might also partly reflect the relative

613   abundances of these elements. However, this appears to be insignificant given that measured

614   concentrations of these elements are extremely low (concentrations of K_2O, Fe_2O_3, and TiO_2

615   are 0–0.12%, 0.03–0.24%, and 0–0.02%, respectively; Fig. S4, Table S3). Other elements,

616   seemingly present as trace amounts of clay, lining pores in the fault breccia (Fig. 7, Table

617   S3), are also an insignificant contributor to variations in ^{36}Cl concentrations. For the Sparta

618   fault at Anogia, quartz embedded in the fault breccia may be the key mineralogical impurity

619   that is likely contributing variance to the ^{36}Cl concentrations, which in turn impacts our

620   ability to obtain unequivocal dates of individual earthquakes.

621

622   **5.4 Interpretation of REE-Y distributions and implications for paleoseismicity**

623   REE-Y cannot be used to infer imprints of former soil profiles on the Sparta fault at Anogia.

624   Petrographic analyses indicate that the Sparta fault scarp is composed of a protocataclasite

625   consisting of calcite clasts derived from the host limestone, microcrystalline calcite cement,

626   and quartz (Figs. 6, 7). Furthermore, EDS analysis indicates that trace amounts of clay, such

627   as illite, are lining pores where microcrystalline calcite cement and quartz are located (Fig. 8;

628   Carcaillet et al., 2008). We infer that REE-Y are adsorbed onto clay minerals lining pores in

629   the fine-grained matrix of the fault breccia, as indicated by correlations between REE-Y and

630   each of Al, K, Si, and Fe (R^2 = 0.92, 0.87, 0.56, and 0.47, respectively; Fig. S4a-c) and

631   between Y and both Si and Al in the hanging wall colluvium (R^2 = 0.71 and 0.45,

632   respectively; Figs. 12c and S4b,c). Supplementary data from the Kaparelli fault (R^2 = 0.95 for

633   Si; Figs. 1a and S5a) and Magnola fault hanging walls (R^2 = 0.98 for both Si and Al; Fig.

634   S5b,c and electronic appendix to Manighetti et al., 2010) also indicate REE-Y may be

635   adsorbed to clay embedded in limestone fault scarps. These correlations generally contrast

636   with a weaker negative correlation between Y and pH (R^2 = 0.52) for the hanging wall soil on

637   the Sparta Fault (Fig. 12c). Soil pH does not appear to be the dominant control on REE-Y

638   distributions in the Sparta fault scarp, which differs to interpretations on other limestone fault

639   scarps (Carcaillet et al., 2008; Bello et al., 2023).

640

641   We propose a causative relationship between the vertical distributions of REE-Y and clay on

642   the Sparta fault scarp. This reasoning is supported by the following observations:

643   (i)   The Sparta fault scarp REE-Y concentrations are equivalent to (Nuriel et al., 2012;

644   Goodfellow et al., 2017) or higher than those measured elsewhere in platformal

645   limestone (Carcaillet et al., 2008; Mouslopoulou et al., 2011), but Y

646   concentrations are lower in the adjacent hanging wall soil (REE were not

647   measured in the soil; Tables S6, S8).

648   (ii)   If REE-Y exchange between the soil and fault scarp occurs according to the

649   Carcaillet et al. (2008) model, fractionation of LREE and HREE elements is

650   expected. For example, LREE might be preferentially mobilized (Takahashi et al.,

651   2005; Carcaillet et al., 2008), leading to an enrichment of LREE relative to HREE

652   in the fault scarp, where there are peaks in total REE-Y. Conversely, LREE may

653   be depleted relative to HREE where there are troughs in total REE-Y. However,

654   the proportion of LREE to HREE remains confined to a constant range vertically

655   along the subaerial section of Sparta fault scarp (Figs.10b, 11a), is weakly

656   correlated with total REE-Y ($R^2 = 0.36$; Fig. 11b), and is relatively depleted at all

657   measured depths beneath the soil surface (Fig. 10b).

658   (iii)   There is no systematic decrease with distance above the hanging wall in total

659   REE-Y (Fig. 10a, b), in contrast to declining concentrations with distance above

660   the hanging wall on the Magnola fault (Carcaillet et al., 2008).

661   Adsorption of REE-Y onto clay has been observed in regolith (Borst et al., 2020) but has not

662   been previously discussed in the context of interpreting paleoseismicity on limestone fault

663   scarps.

664

665   Although we infer that adsorption of REE-Y onto clay minerals embedded in fault breccia

666   dominates on the Sparta fault, the approximate coincidence of the subsurface peak in scarp

667   LREE/HREE and total REE-Y with the mid-profile peak in soil pH (Figs. 10, 12a, b)

668   provides evidence of REE-Y exchange between the scarp and the soil. However, the

669   consequence is LREE depletion in the scarp, rather than enrichment (Fig. 10b), and it is

670   unclear why this apparent depletion is not replicated on the subaerially exposed scarp. One

671   possibility is that colluvium accumulation postdates the most recent earthquake although, if

672   so, low ^{36}Cl concentrations in the buried scarp surface indicate that the soil accumulation was

673   co-seismic with the last earthquake or accumulated soon afterwards. It is also unclear why

674   colluvium would accumulate only after the most recent earthquake. An alternative possibility

675   is that a superficial LREE-depleted zone has been eroded from the subaerial scarp surface

676   through dissolution. This would imply erosion of centimeters of scarp surface since the last

677   known earthquake on the Sparta fault at 464 B.C.E. (an erosion rate of 0.01 mm yr^{-1} over the

678   past 2500 years would remove 2.5 cm of scarp surface). Yet another possibility is that

679   perhaps more time is required to increase LREE to concentrations seen on the subaerial scarp

680   surface, but 2500 years have already passed since the most recent known earthquake and

681   maximum REE-Y enrichment has been inferred to occur within 500 years on the Spilli and

682   Magnola faults (Manighetti et al., 2010; Mouslopoulou et al., 2011). Alternatively, LREE

683   enrichment occurs after scarp exhumation, perhaps through exchange with aeolian dust

684   fallout, as has been observed in Dead Sea halite (Censi et al., 2023). Such dust inputs may

685   supply REE-Y (Yang et al., 2007), as indicated by the correlation between Y and Si in the

686 hanging wall colluvium (Fig. 12b, c), contribute fine-grained mineral soil to the hanging wall

687 colluvium, and may lower soil pH through buffering locally-sourced $CaCO_3$. However, given

688 that inputs of Saharan dust are ubiquitous throughout the Mediterranean (Stuut et al., 2009)

689 and can comprise a large component of soils in the region (Muhs et al., 2010; Styllas et al.,

690 2023), similar patterns of LREE depletion in the soil-covered scarp surface relative to the

691 subaerial scarp surface are expected to have been observed elsewhere, which is not the case

692 (Carcaillet et al., 2008; Manighetti et al., 2010; Mouslopoulou et al., 2011; Tesson et al.,

693 2016; Bello et al., 2023).

694

695 For the Sparta fault scarp, the presence of clay likely relates to fault breccia formation at

696 considerable depths beneath the Earth's surface, rather than subaerial weathering processes.

697 The formation of protocataclasite occurs beneath the Earth's surface at depths that may range

698 from meters to up to thousands of meters. A model for this involves fluids moving along the

699 Sparta fault, primarily associated with seismic events. These fluids dissolve $CaCO_3$ from the

700 host-limestones and potentially also silicate minerals from psammitic and pelitic

701 (meta)sediments, where they are dissected by the fault. In association with variations in

702 temperature and pressure along the fault, chemical saturation of these fluids results in

703 precipitation of clay, quartz, and microcrystalline calcite, which cements clasts of host-rock

704 derived limestone into the fault breccia. Subsequent faulting re-fractures the breccia and

705 particle comminution over time produces quartz grains that are rounded-to-angular in shape,

706 randomly oriented, and <50 μm (Figs. 6, 8). The fault breccia may also have undergone

707 multiple generations of microcrystalline calcite re-cementing from re-circulating fluids. As an

708 alternative to a dissolution-precipitation model, clay and quartz emplacement may involve

709 fluid entrainment of particles and grains from clay- and quartz-bearing sedimentary units

710 during faulting, as has been observed elsewhere (e.g., Darwin, 1840; Roy, 1946; Brandon,

711 1972; Röshoff and Cosgrove, 2002). This process may also be accompanied by comminution

712 of fault-zone quartz grains derived from psammitic rocks. We tentatively exclude a

713 contemporary aeolian source for the clay and quartz because there is no documented

714 mechanism to transport clay particles and quartz grains from the soil to centimeters into a

715 fault scarp. We cannot distinguish soil to scarp clay and quartz migrations on the Sparta fault

716 which has been observed, for example, at the micrometer scale in surface coatings on the

717 Magnola fault, because that scarp is comprised of pure carbonate (Carcaillet et al., 2008). It is

718 likely that limestone fault scarps are generally composed of fault breccias (Agosta and Aydin,

719 2006; Carcaillet et al., 2008; Nuriel et al., 2012) and that where a fault intersects varying

720 lithologies, chemical and mineralogical heterogeneities may occur in the fault breccia, as

721 observed on the Sparta fault. Where they occur, these heterogeneities may control the spatial

722 distribution of REE-Y, independent of any spatial reorganization of REE-Y attributable to

723 subaerial weathering. If, as we infer, the spatial patterning of REE-Y, quartz, and clay is

724 inherited from depth, the observed wave-like signal (Figs. 7, 10) may reflect sorting and

725 cementing of breccia around surface asperities on the fault plane. The resulting infilling of

726 depressions with fault gauge may create a successively more polished and localized fault

727 plane along which friction is lowered, thereby permitting larger slip (i.e., larger earthquakes)

728 along the fault (Sagy and Brodsky, 2009). Whereas REE-Y concentrations do not appear to

729 be a reliable indicator of Holocene paleoseismicity of the Sparta fault, they may instead

730 reveal processes that localize slip to a discrete fault plane.

731

732 Whereas the Sparta Fault displays concentrations of clay and quartz impurities that are much

733 higher than on other reported limestone fault scarps, three general implications emerge for

734 using REE-Y in making inferences of paleoseismicity. Firstly, the potential control on REE-

735 Y distributions of even trace amounts of non-calcite impurities in the breccia comprising fault

736   scarps should be considered through analyses of thin sections in addition to scarp chemistry.

737   Secondly, soil acidity and REE-Y enrichment, including any resulting exchange with the

738   buried scarp, may peak some tens of centimeters below the colluvium surface. Peaks in REE-

739   Y concentrations on subaerial fault scarp surfaces may not therefore reflect former soil

740   surfaces, even if there is soil-scarp exchange of REE-Y. In addition, the Sparta fault scarp

741   REE-Y data indicate that it may be rewarding to focus on up-scarp variations in LREE/HREE

742   ratios rather than on REE-Y concentrations, because these may be a sensitive indicator of

743   REE-Y exchange processes occurring beneath soil covers (Fig 10b). Lastly, relationships

744   between REE-Y distributions and soil mineralogy should be more closely assessed, in

745   addition to the commonly modelled and studied effects of pH (e.g., Carcaillet et al., 2008;

746   Manighetti et al., 2010; Mouslopoulou et al., 2011; Moraetis et al., 2015, 2023; Tesson et al.,

747   2016; Bello et al., 2023). Fine grained mineral inputs through aeolian dust fallout comprise

748   substantial volumes of Mediterranean soils (Muhs et al., 2010; Styllas et al., 2023) and

749   decadal to millennial variations in dust fluxes may directly impact on REE-Y distributions in

750   hanging wall soils and potentially in scarp surfaces, in locations where soil-scarp REE-Y

751   exchange is important. These fluctuations may contribute to REE-Y patterns in soils that are

752   difficult to predict and in scarp surfaces reflect (climatic and pedogenic) processes that may

753   complicate potential paleoseismic inferences.

754

755   Moraetis et al. (2023) consider REE-Y analyses an established method in paleoseismicity.

756   Our detailed study errs towards caution; there remain important uncertainties regarding

757   processes of REE-Y enrichment and depletion in limestone fault scarps. Indeed, we maintain

758   that there is considerable uncertainty regarding how the resulting patterns should be

759   interpreted with respect to paleoseismicity. Fundamentally, it remains unclear how far into

760   buried scarp surfaces the REE-Y can be adsorbed from soil or incorporated into calcite

through dissolution-precipitation. A dissolution rate of 0.001 mm yr^{-1} will erode 1 cm from a

subaerially exposed scarp surface over 10 000 years, which is about the timescale considered

to be relevant to assessing full seismic cycles and therefore making accurate assessments of

paleoseismicity (Mouslopoulou et al., 2012; Tesson et al., 2016). Even such a slow rate of

subaerial scarp dissolution will therefore remove any REE-Y signals inherited from former

soil cover unless that exchange extends to centimeters into the scarp.

6 Conclusion

Modelling of ^{36}Cl data from the Sparta fault at Anogia, Greece, indicates an increase in

average slip rate during exhumation of the scarp from 0.8–0.9 mm yr^{-1} between 7.7 and 6.5

kyr ago to 1.0 mm yr^{-1} between 6.5 and 2.5 kyr ago (the timing if the historic 464 B.C.E.

earthquake). Average exhumation of the entire scarp is 0.7– 0.8 mm yr^{-1}. Modelling does not

indicate that earthquakes may have contributed to exhumation of the Sparta fault since 464

B.C.E.

The Sparta fault scarp is impure; it is composed of fault breccia, which contains quartz and

clay-lined pores in addition to calcite. The vertical distribution of REE-Y is highly correlated

with the pore-clay and may indicate processes that localize slip to a discrete fault plane deep

below the ground surface. The potential exchange of REE-Y between the hanging wall

colluvium and the adjacent footwall scarp is overwhelmed at this site by REE-Y attached to

the pore clays inherited from depth. Because of this, Holocene earthquakes and their slip

distances and magnitudes cannot be inferred for the Sparta fault from REE-Y concentrations.

Whereas this is probably true also for similar impure limestone fault scarps elsewhere, other

controls on REE-Y distributions, in addition to hanging wall soil pH, should be evaluated in

785   attempting paleoseismic inferences more generally from normal fault scarps developed in

786   limestone.

787

788 **Author contribution**
789 AS and APS conceived the study and acquired the funding for RF. BWG, APS, and AS
790 supervised RF. APS, AS, BWG, MWC, and RF participated in fieldwork. RF conducted the
791 analysis of scarp composition and made initial interpretations. BWG performed additional
792 analyses and earthquake modelling, and wrote the manuscript. GC led the laboratory
793 preparation of samples for ^{36}Cl measurement, together with BWG, and calculated ^{36}Cl
794 concentrations from the AMS data. All authors contributed to data interpretation and
795 manuscript editing.
796

797 **Competing interests**
798 Arjen P. Stroeven is a member of the editorial board for Solid Earth.
799

800 **Acknowledgements**
801 We thank Mikael Amlert for his assistance with field safety and sampling, Giorgos Maneas,
802 station manager of the Navarino Environmental Observatory (NEO), for his extensive
803 assistance with field logistics, and our deceased friend, Dan Zetterberg, Department of
804 Geological Sciences, Stockholm University, for his assistance with thin section preparations.
805 This project was funded by the Stockholm University Research School for teachers focusing
806 on Natural Hazards financed by the Swedish Research Council and by a grant from NEO. We
807 gratefully acknowledge funding for fieldwork from the Swedish Society for Anthropology
808 and Geography Andreé Fund to Fritzon.
809

810 **References**
811 Agosta, F. and Aydin, A.: Architecture and deformation mechanism of a basin bounding
812   normal fault in Mesozoic platform carbonates, central Italy. Journal of Structural
813   Geology, 28, 1445–1467, 2006.
814 Armijo, R., Lyon-Caen, H., and Papanastassiou, D.: A possible normal-fault rupture for the
815   464 BC Sparta earthquake. Nature, 351, 137–139, 1991.
816 Bello, S., Perna, M.G., Consalvo, A., Brozzetti, F., Galli, P., Cirillo, D., Andrenacci, C.,
817   Tangari, A.C., Carducci, A., Menichetti, M., Lavecchia, G., Stoppa, F., and Rosatelli, G.:
818   Coupling rare earth element analyses and high-resolution topography along fault scarps to
819   investigate past earthquakes: A case study from the Southern Apennines (Italy).
820   Geosphere, 19, 1348–1371, 2023.
821 Benedetti, L., Finkel, R., Papanastassiou, D., King, G., Armijo, R., Ryerson, F., Farber, D.,
822   and Flerit, F.: Post-glacial slip history of the Sparta fault (Greece) determined by ^{36}Cl
823   cosmogenic dating: Evidence for non-periodic earthquakes. Geophysical Research
824   Letters, 29, 1246, 2002.
825 Benedetti, L., Manighetti, I., Gaudemer, Y., Finkel, R., Malavieille, J., Pou, K., Arnold, M.,
826   Aumaître, G., Bourlès, D. and Keddadouche, K.: Earthquake synchrony and clustering on
827   Fucino faults (Central Italy) as revealed from in situ ^{36}Cl exposure dating. Journal of
828   Geophysical Research, Solid Earth, 118, 4948–4974, 2013.
829 Borst, A. M., Smith, M. P., Finch, A. A., Estrade, G., Villanova-de-Benavent, C., Nason, P.,
830   Marquis, E., Horsburgh, N. J., Goodenough, K. M., Xu, C., Kynický, J. and Geraki,

831   K.: Adsorption of rare earth elements in regolith-hosted clay deposits. Nature
832   Communications, 11, 4386, 2020.
833 Brandon, A: Clastic dykes in the Namurian shales of County Leitrim, Republic of Ireland.
834   Geological Magazine, 109, 361–367, 1972.
835 Bubeck, A., Wilkinson, M., Roberts, G. P., Cowie, P. A., McCaffrey, K. J. W., Phillips, R.
836   and Sammonds, P.: The tectonic geomorphology of bedrock scarps on active normal
837   faults in the Italian Apennines mapped using combined ground penetrating radar and
838   terrestrial laser scanning. Geomorphology, 237, 38–51, 2015.
839 Carcaillet, J., Manighetti, I., Chauvel, C., Schlagenhauf, A., and Nicole, J.-M.: Identifying
840   past earthquakes on an active normal fault (Magnola, Italy) from the chemical analysis of
841   its exhumed carbonate fault plane. Earth and Planetary Science Letters, 271, 145–158,
842   2008.
843 Censi, P., Sirota, I., Zuddas, P., Lensky, N.G., Crouvi, O., Cangemi, M. and Piazzese, D.:
844   Rare earths release from dissolving atmospheric dust and their accumulation into
845   crystallising halite: The Dead Sea example. Science of the Total Environment, 875,
846   162682, 2023.
847 Cowie, P.A., Phillips, R.J., Roberts, G.P., McCaffrey, K., Zijerveld, L.J.J., Gregory, L.C.,
848   Faure Walker, J., Wedmore, L.N.J., Dunai, T.J., Binnie, S.A., Freeman, S.P.T.H.,
849   Wilcken, K., Shanks, R.P., Huismans, R.S., Papanikolaou, I., Michetti, A.M. and
850   Wilkinson, M.: Orogen-scale uplift in the central Italian Apennines drives episodic
851   behaviour of earthquake faults. Scientific Reports, 7, 44858, 2017.
852 Darwin, C: Geological observations in the volcanic islands and parts of South America
853   visited during the voyage of H.M.S. Beagle. London, 1840.
854 Dawood, R., Matmon, A., Benedetti, L., ASTER Team and Siman-Tov, S.: Multi-segment
855   earthquake clustering as inferred from ^{36}Cl exposure dating, the Bet Kerem fault system,
856   northern Israel. Tectonics, 43, e2023TC007953, 2024.
857 Dramis, F, and Blumetti, A.M.: Some considerations concerning seismic geomorphology and
858   paleoseismology. Tectonophysics, 408, 177–191, 2005.
859 Evans, J.M, Stone, J.O.H., Fifield, L.K., and Cresswell, R.G.: Cosmogenic chlorine-36
860   production in K-feldspar. Nuclear Instruments and Methods in Physics Research B, 123,
861   334–340, 1997.
862 Fink, D., Vogt, S., and Hotchkis, M.: Cross-sections for ^{36}Cl from Ti at E_p = 35–150 MeV:
863   Applications to in-situ exposure dating. Nuclear Instruments and Methods in Physics
864   Research B, 172, 861–866, 2000.
865 Friedrich, A. M., Wernicke, B. P., Niemi, N. A., Bennett, R.A. and Davis, J.L.: Comparison
866   of geodetic and geologic data from the Wasatch region, Utah, and implications for the
867   spectral character of Earth deformation at periods of 10 to 10 million years, Journal of
868   Geophysical Research: Solid Earth, 108, 2199, 2003.
869 Godey, S., Bossu, R., and Guilbert, J.: Improving the Mediterranean seismicity picture thanks
870   to international collaborations. Physics and Chemistry of the Earth, Parts A/B/C, 63, 3–
871   11, 2013.
872 Goodall, H. J., Gregory, L. C., Wedmore, L. N. J., McCaffrey, K. J. W., Amey, R. M. J.,
873   Roberts, G. P., Shanks, R.P., Phillips, R.J. and Hooper, A. Determining histories of slip
874   on normal faults with bedrock scarps using cosmogenic nuclide exposure data. Tectonics,
875   40, e2020TC006457, 2021.
876 Goodfellow, B.W., Viola, G., Bingen, B., Nuriel, P. and Kylander-Clark, A.: Paleocene
877   faulting in SE Sweden from U-Pb dating of slickenfiber calcite. Terra Nova, 29, 321–328,
878   2017.
879 Gürpinar, A.: The importance of paleoseismology in seismic hazard studies for critical
880   facilities. Tectonophysics, 408, 23–28, 2005.

881 Hastings, W.K.: Monte Carlo sampling methods using Markov chains and their applications.
882   Biometrika, 57, 97–109, 1970.

883 Hickson, C.J. and Juras, S.J.: Sample contamination by grinding. Canadian Mineralogist, 24,
884   585–589, 1986.

885 Hutchison, C.S.: Laboratory Handbook of Petrographic Techniques. Wiley-Interscience, New
886   York, 527 pp, 1974.

887 Iezzi, F., Roberts, G., Faure Walker, J., Papanikolaou, I., Ganas, A., Deligiannakis, G., Beck,
888   J., Wolfers, S. and Gheorghiu, D.: Temporal and spatial earthquake clustering revealed
889   through comparison of millennial strain-rates from ^{36}Cl cosmogenic exposure dating and
890   decadal GPS strain-rate. Scientific Reports, 11, 23320, 2021.

891 Institute for Geology and Subsurface Research: Sparti Sheet, photogeological map of Greece,
892   1969.

893 Jolivet, L., Faccenna, C., Huet, B., Labrousse, L., Le Pourhiet, L., Lacombe, O., Lecomte, E.,
894   Burov, E., Denèle, Y., Brun, J.-P., Philippon, M., Paul, A., Salaün, G., Karabulut, H.,
895   Piromallo, C., Monié, P., Gueydan, F., Okay, A.I., Oberhänsli, R., Pourteau, A., Augier,
896   R., Gadenne, L. and Driussi, O.: Aegean tectonics: Strain localisation, slab tearing and
897   trench retreat. Tectonophysics, 597–598, 1–33, 2013.

898 Lifton, N.A., Bieber, J.W., Clem, J.M., Duldig, M.L., Evenson, P., Humble, J.E. and Pyle, R.:
899   Addressing solar modulation and long-term uncertainties in scaling secondary cosmic
900   rays for in situ cosmogenic nuclide applications. Earth and Planetary Science Letters,
901   239, 140–161, 2005.

902 Lifton, N.A., Sato, T. and Dunai, T.J.: Scaling in situ cosmogenic nuclide production rates
903   using analytical approximations to atmospheric cosmic-ray fluxes. Earth and Planetary
904   Science Letters, 386, 149–160, 2014.

905 Lifton, N.A., Smart, D.F. and Shea, M.A.: Scaling time-integrated in situ cosmogenic nuclide
906   production rates using a continuous geomagnetic model. Earth and Planetary Science
907   Letters, 268, 190–201, 2008.

908 Manighetti, I., Boucher, E., Chauvel, C., Schlagenhauf, A. and Benedetti, L.: Rare earth
909   elements record past earthquakes on exhumed limestone fault planes. Terra Nova, 22,
910   477–482, 2010.

911 Marrero, S.M., Phillips, F.M., Caffee, M.W. and Gosse, J.C.: CRONUS-Earth cosmogenic
912   ^{36}Cl calibration. Quaternary Geochronology, 31, 199–219, 2016.

913 McCalpin, J.P.: Paleoseismology, Academic press, 613 pp., 2009.

914 McDonough, W.F. and Sun, S.-s.: The composition of the Earth. Chemical Geology, 120,
915   223–253, 1995.

916 Metropolis, N., Rosenbluth, A. W., Rosenbluth, M. N., Teller A. H. and Teller, E.: Equation of state
917   calculations by fast computing machines. Journal of Chemical Physics, 21, 1087–1092, 1953.

918 Michetti, A.M., Audemard, F.A. and Marco, S.: Future trends in paleoseismology: Integrated
919   study of the seismic landscape as a vital tool in seismic hazard analyses Tectonophysics,
920   408, 3–21, 2005.

921 Mitchell, S.G., Matmon, A., Bierman, P.R., Enzel, Y., Caffee, M. and Rizzo, D.:
922   Displacement history of a limestone normal fault scarp, northern Israel, from cosmogenic
923   ^{36}Cl. Journal of Geophysical Research: Solid Earth, 106, 4247–4264, 2001.

924 Moore, A. K. and Granger, D. E.: Calibration of the production rate of cosmogenic ^{36}Cl from
925   Fe. Quaternary Geochronology, 51, 87–98, 2019.

926

927 Moraetis, D., Mouslopoulou, V., Pratikakis, A., Begg J. and Pracejus, B.: The mechanism of
928   REE-Y impregnation on active carbonate normal fault scarps. Applied Geochemistry,
929   155, 105703, 2023.

Mouslopoulou, V., Moraetis, D. and Fassoulas, C.: Identifying past earthquakes on carbonate faults: Advances and limitations of the 'Rare Earth Element' method based on analysis of the Spili Fault, Crete, Greece. Earth and Planetary Science Letters, 309, 45–55, 2011.

Mouslopoulou, V., Nicol, A., Walsh, J.J., Begg, J.G., Townsend, D.B. and Hristopulos, D.T.: Fault-slip accumulation in an active rift over thousands to millions of years and the importance of paleoearthquake sampling, Journal of Structural Geology, 36, 71–80, 2012.

Mozafari, N., Özkaymak, C., Sümer, Ö, Tikhomirov, D., Uzel, B., Yeşilyurt, S., Ivy-Ochs, S., Vockenhuber, C., Sözbilir, H. and Akçar, N.: Seismic history of western Anatolia during the last 16 kyr determined by cosmogenic ^{36}Cl dating. Swiss Journal of Geosciences, 115, 5, 2022.

Muhs, D.R., Budahn, J., Avila, A., Skipp, G., Freeman, J. and Patterson, D.: The role of African dust in the formation of Quaternary soils on Mallorca, Spain and implications for the genesis of Red Mediterranean soils. Quaternary Science Reviews, 29, 2518–2543, 2010.

Muzikar, P., Elmore, D. and Granger, D.E.: Accelerator mass spectrometry in geologic research. Geological Society of America Bulletin, 115, 643–654, 2003.

Nuriel, P., Rosenbaum, G., Zhao, J.-X., Feng, Y., Golding, S.D., Villemant, B. and Weinberger, R.: U-Th dating of striated fault planes. Geology, 40, 647–650, 2012.

Palumbo, L., Benedetti, L., Bourlès, D., Cinque, A. and Finkel, R.: Slip history of the Magnola fault (Apennines, Central Italy) from ^{36}Cl surface exposure dating: evidence for strong earthquakes over the Holocene. Earth and Planetary Science Letters, 225, 163–176, 2004.

Papanikolaou, I.D., Roberts, G.P., Deligiannakis, G., Sakellariou, A. and Vassilakis, E.: The Sparta Fault, Southern Greece: From segmentation and tectonic geomorphology to seismic hazard mapping and time dependent probabilities. Tectonophysics, 597–598, 85–105, 2013.

Pope, R.J. and Wilkinson, K.N.: Reconciling the roles of climate and tectonics in Late Quaternary fan development on the Spartan piedmont, Greece. In: A.M. Harvey, A.E. Mather, and M. Stokes, (Eds), Alluvial Fans: Geomorphology, Sedimentology, Dynamics. Geological Society, London, Special Publications, 251, 133–152, 2005.

Röshoff, K. and Cosgrove, J.: Sedimentary dykes in the Oskarshamn-Västervik area. A study of the mechanism of formation. SKB Report R-02-37, 98 pp, 2002.

Roy, C.J.: Clastic dykes of the Pikes Peak region. Abstract. Geological Society of America Bulletin, 57, 1226, 1946.

Sagy, A. and Brodsky, E.E.: Geometric and rheological asperities in an exposed fault zone. Journal of Geophysical Research, 114, B02301, 2009.

Schlagenhauf, A., Gaudemer, Y., Benedetti, L., Manighetti, I., Palumbo, L., Schimmelpfennig, I., Finkel, R. and Pou, K.: Using *in situ* Chlorine-36 cosmonuclide to recover past earthquake histories on limestone normal fault scarps: a reappraisal of methodology and interpretations. Geophysical Journal International, 182, 36–72, 2010.

Sharma, P., Kubik, P.W., Fehn, U., Gove, H.E., Nishiizumi, K. and Elmore, D.: Development of ^{36}Cl Standards for AMS. Nuclear Instruments & Methods in Physics Research Section B-Beam Interactions with Materials and Atoms, 52, 410–415, 1990.

Sikora, F.J. and Moore, K.P. (Eds.): Soil Test Methods from the Southeastern United States. Southern Cooperative Series Bulletin, 419, 211 p., 2014.

Stone, J.O.: Air pressure and cosmogenic isotope production. Journal of Geophysical Research: Solid Earth, 105, 23753–23759, 2000.

977 Stone, J.O.: Terrestrial chlorine-36 production from spallation of iron. In: Abstract of 10th
978   International Conference on Accelerator Mass Spectrometry, Berkeley, California, USA.,
979   2005.

980 Stone, J.O., Allan, G.L., Fifield, L.K. and Cresswell, R.G.: Cosmogenic chlorine-36 from
981   calcium spallation. Geochimica et Cosmochimica Acta, 60, 679–692, 1996.

982 Stuut, J.-B., Smalley, I. and O'Hara-Dhand, K.: Aeolian dust in Europe: African sources and
983   European deposits. Quaternary International, 198, 234–245, 2009.

984 Styllas, M., Pennos, C., Persoiu, A., Godelitsas, A., Papadopoulou, L., Aidona, E.,
985   Kantiranis, N., Ducea, M.N., Ghilardi, M. and Demory, F.: Aeolian dust accretion
986   outpaces erosion in the formation of Mediterranean alpine soils. New evidence from the
987   periglacial zone of Mount Olympus, Greece. Earth Surface Processes and Landforms, 48,
988   3003–3021, 2023.

989 Takahashi, Y., Chatellier, X., Hattori, K.H., Kato, K. and Fortin, D.: Adsorption of rare earth
990   elements onto bacterial cell walls and its implication for REE sorption onto natural
991   microbial mats. Chemical Geology, 219, 53–67, 2005.

992 Tesson, J., Pace, B., Benedetti, L., Visini, F., Delli Rocioli, M., Arnold, M., Aumaître, G.,
993   Bourlès, D.L. and Keddadouche, K.: Seismic slip history of the Pizzalto fault (central
994   Apennines, Italy) using in situ-produced ^{36}Cl cosmic ray exposure dating and rare earth
995   element concentrations. Journal of Geophysical Research: Solid Earth, 121, 1983–2003,
996   2016.

997 Tikhomirov D., Amiri, N.M., Ivy-Ochs, S., Alfimov, V., Vockenhuber, C., Akçar, N.: Fault
998   Scarp Dating Tool – a MATLAB code for fault scarp dating using in-situ chlorine-36
999   supplemented with datasets of Yavansu and Kalafat faults. Data in brief, 26, 104476,
1000   2019.

1001 Tesson, J. and Benedetti, L.: Seismic history from in situ ^{36}Cl cosmogenic nuclide data on
1002   limestone fault scarps using Bayesian reversible jump Markov chain Monte Carlo.
1003   Quaternary Geochronology, 52, 1–20, 2019.

1004 Tucker, G. E., McCoy, S. W., Whittaker, A. C., Roberts, G. P., Lancaster, S. T. and Phillips,
1005   R.: Geomorphic significance of postglacial bedrock scarps on normal-fault footwalls.
1006   Journal of Geophysical Research: Solid Earth, 116, F01022, 2011.

1007 Wallace, R. E.: Grouping and migration of surface faulting and variations in slip rates on
1008   faults in the Great Basin province. Bulletin of the Seismological Society of America, 77,
1009   868–876, 1987.

1010 Woodcock, N.H. and Mort, K.: Classification of fault breccias and related fault rocks.
1011   Geological Magazine, 145, 435–440, 2008.

1012 Yang, X., Liu, Y., Li, C., Song, Y., Zhu, H. and Jin, X.: Rare earth elements of aeolian
1013   deposits in Northern China and their implications for determining the provenance of dust
1014   storms in Beijing. Geomorphology, 87, 365–377, 2007.

1015 Zreda, M. and Noller, J. S.: Ages of prehistoric earthquakes revealed by cosmogenic
1016   chlorine-36 in a bedrock fault scarp at Hebgen Lake. Science, 282, 1097–1099, 1998.

1017 **Table 1:** Parameters for MCMC modelling of slip rate.

α (°)	β (°)	γ (°)	Scarp (cm)	Buried scarp (cm)	ρ_{rock} (g cm^{-3})	$\rho_{colluvium}$ (g cm^{-3})	^{36}Cl P$_o$ (at. g^{-1} yr^{-1})	ε (mm yr^{-1})	Pre (kyr)	Scarp age (kyr ± 1σ)	Elapsed time (kyr ± 1σ)
32	62	20	650	80	2.6	1.9	59.4 ± 4.3	0.02	7.7	8.0 ± 1.5	2.5 ± 1.0

1018

1019 α is hanging wall colluvial surface dip angle; β is scarp dip angle; γ is the dip angle of the hillslope above the fault scarp; ε is
1020 scarp erosion rate; Pre is pre-exposure; Scarp age is the initial estimate of exhumation of the oldest (highest) part of the scarp;
1021 Elapsed time is the estimated duration following the last earthquake. The ^{36}Cl production rate of 59.4 ± 4.3 at g^{-1} yr^{-1} is taken
1022 from Schlagenhauf et al. (2010), calculated from Lifton et al. (2005).
1023 When using the ^{36}Cl production rate of 48.8 ± 3.5 at g^{-1} yr^{-1} from Stone et al. (1996), Pre is 10.6 kyr; otherwise, all other
1024 parameters are fixed.

1025

1026 **Table 2:** Slip rates for the Sparta fault at Anogia from the best Markov chain Monte Carlo
1027 models (n = 10,000), for end-member ^{36}Cl production rates and varying number of model
1028 earthquakes.

Slip rate calculation model (^{36}Cl production rate, number of earthquakes)	Mean slip rate (mm yr^{-1})	MAP slip rate (mm yr^{-1})
48.8, 3 earthquakes, to present	0.72	0.70
48.8, 5 earthquakes, to present	0.71	0.70
48.8, 6 earthquakes, to present	0.70	0.70
59.4, 3 earthquakes, to present	0.79	0.76
59.4, 5 earthquakes, to present	0.78	0.75
59.4, 6 earthquakes, to present	0.77	0.75
48.8, 3 earthquakes, to 464 B.C.E. earthquake	1.10	1.08
48.8, 5 earthquakes, to 464 B.C.E. earthquake	1.11	1.11
48.8, 6 earthquakes, to 464 B.C.E. earthquake	1.10	1.11
59.4, 3 earthquakes, to 464 B.C.E. earthquake	1.21	1.15
59.4, 5 earthquakes, to 464 B.C.E. earthquake	1.22	1.16
59.4, 6 earthquakes, to 464 B.C.E. earthquake	1.22	1.18
48.8, 5 earthquakes, 0–3.7 m on fault scarp	0.95	0.94
59.4, 5 earthquakes, 0–3.7 m on fault scarp	1.03	0.96
48.8, 5 earthquakes, 3.7–6.5 m on fault scarp	0.83	0.80
59.4, 5 earthquakes, 3.7–6.5 m on fault scarp	0.92	0.92

1029 MAP is maximum a posteriori probability

Figures
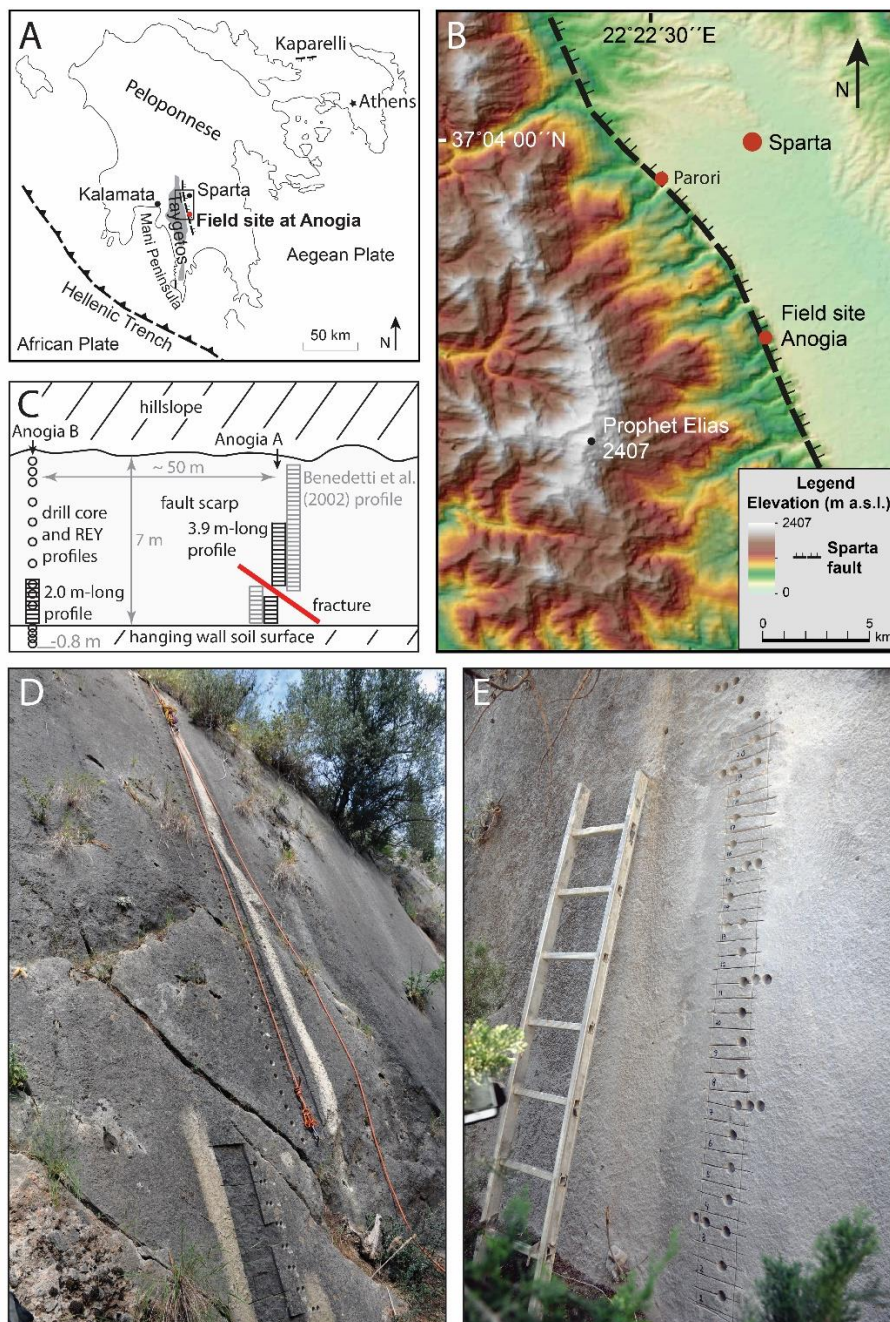
Fig. 1: Study site. A. The study site location in Peloponnese, Greece. Key tectonic features are shown. Box indicates location of panel B. B. The location of the Sparta fault, separating the Taygetos Mountains from the Sparta basin. The location of the Anogia field site used both in this study and in Benedetti et al. (2002) is shown. Benedetti et al. (2002) located a second sampling transect at Parori (also shown). The digital elevation model has a 24 m resolution and is derived from ASTER GDEM (GDEM2), which is a product of NASA and METI (Japan). C. Schematic diagram of the Sparta fault scarp at Anogia, showing the locations of our vertical ^{36}Cl and REE-Y sampling transects, and the ^{36}Cl sampling transect of Benedetti et al. (2002). D. Photograph showing the location of our 3.9 m-long profile, prior to sampling. The existing sample scar is from Benedetti et al. (2002). E. Photograph showing the location of our REE-Y and drill core profiles, after sampling, and our 2.0 m long profile, before sampling.
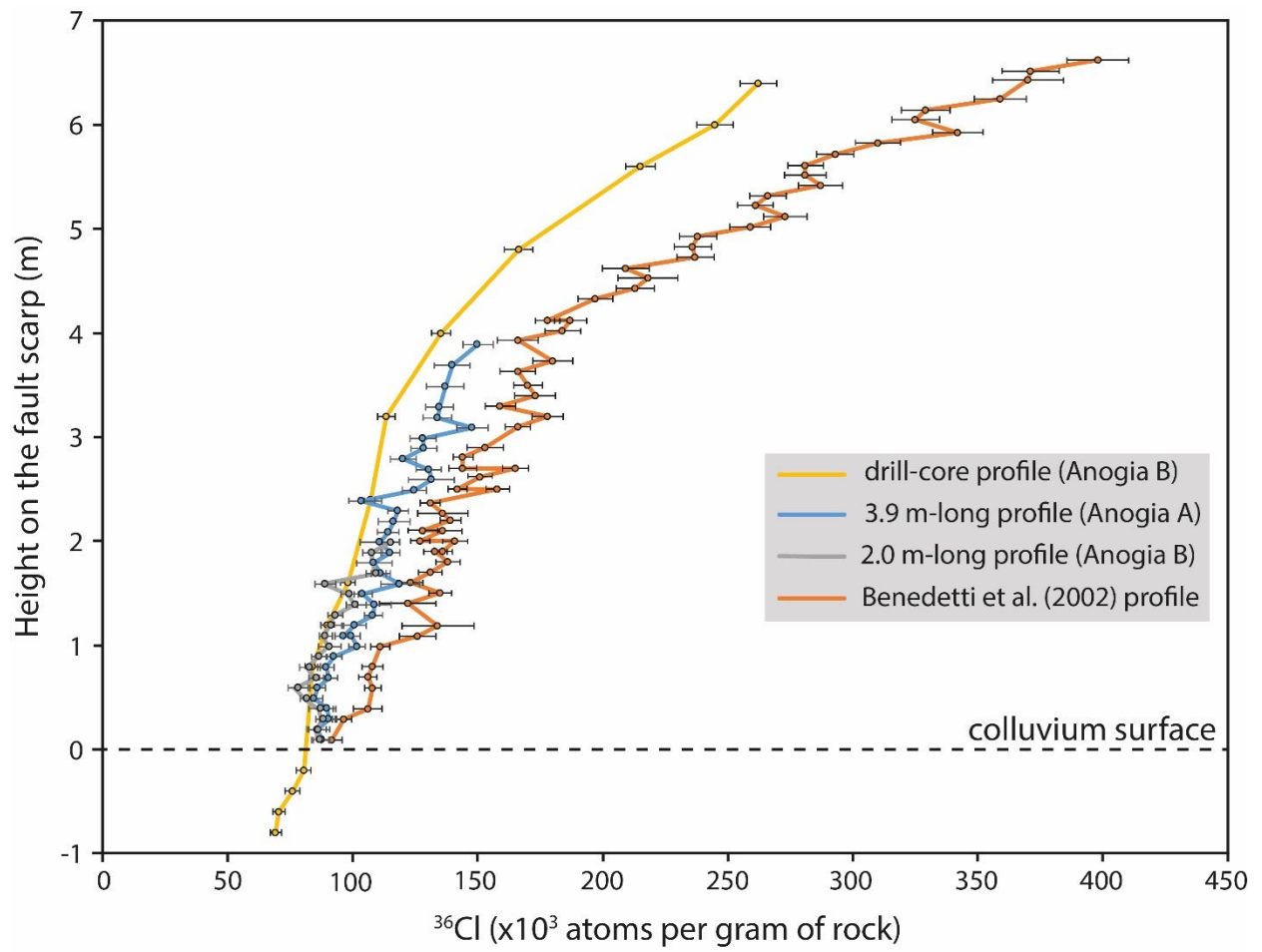
Fig. 2: Sparta fault ^{36}Cl concentration profiles. Error bars indicate 1σ measurement uncertainties..
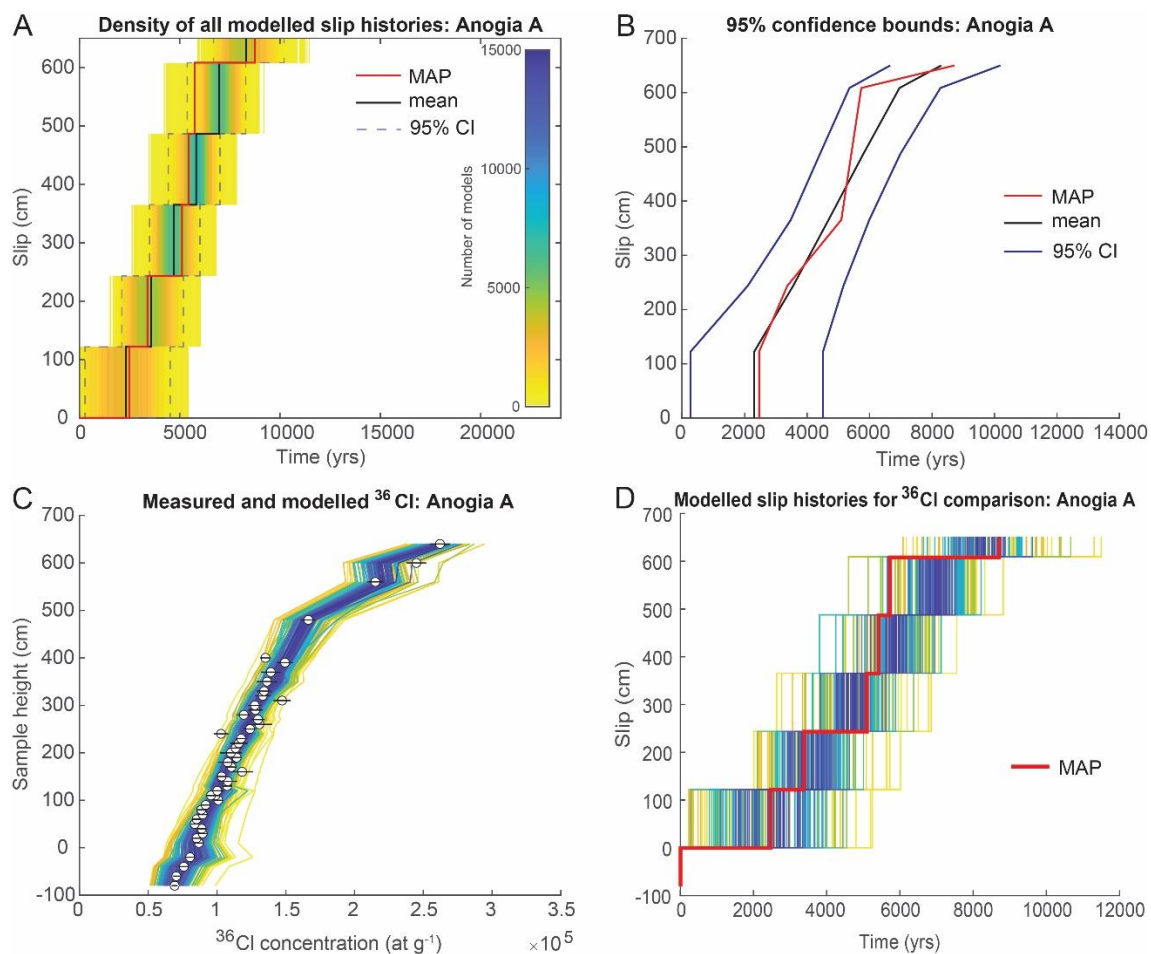
1049

1050

1051

Fig. 3: Markov chain Monte Carlo (MCMC) model fits to measured ^{36}Cl concentrations and model slip histories, Anogia A + drill core profile. Slip accumulation is shown for five model earthquakes that each exhume the same vertical length of scarp rather than reflecting the magnitude and timing of historical earthquakes. The red line in panels a, b, and d is the maximum a posteriori probability (MAP) estimation model, which is the maximum likelihood multiplied by the prior probability based on scarp age. Each panel includes 160k iterations, following removal of a burn-in of the first 40k iterations. A. Histogram showing the distribution of accepted model slip histories in slip-space versus time. The density of overlapping models increases from warm to cool colours. The mean model and 95% confidence bounds are also shown. B. The 95% confidence bounds of the smoothed model distribution (black lines) calculated for age at each step in the slip. The mean (black line) and MAP (red line) slip histories are also plotted. C. Model fits to measured ^{36}Cl concentrations (circles). The coloured lines represent a selection of 160 model fits from low- (yellow) to high-probability (blue) at equal intervals (1000) through the distribution. The black lines indicate 1σ measurement uncertainties. D. Slip histories through five model earthquakes corresponding to MCMC fits shown in panel c. Results are shown for a ^{36}Cl production rate of 59.4 ± 4.3 atoms g Ca^{-1} yr^{-1}. Refer to Fig. S2 for equivalent results using a production rate of 48.8 ± 3.5 atoms g Ca^{-1} yr^{-1}.
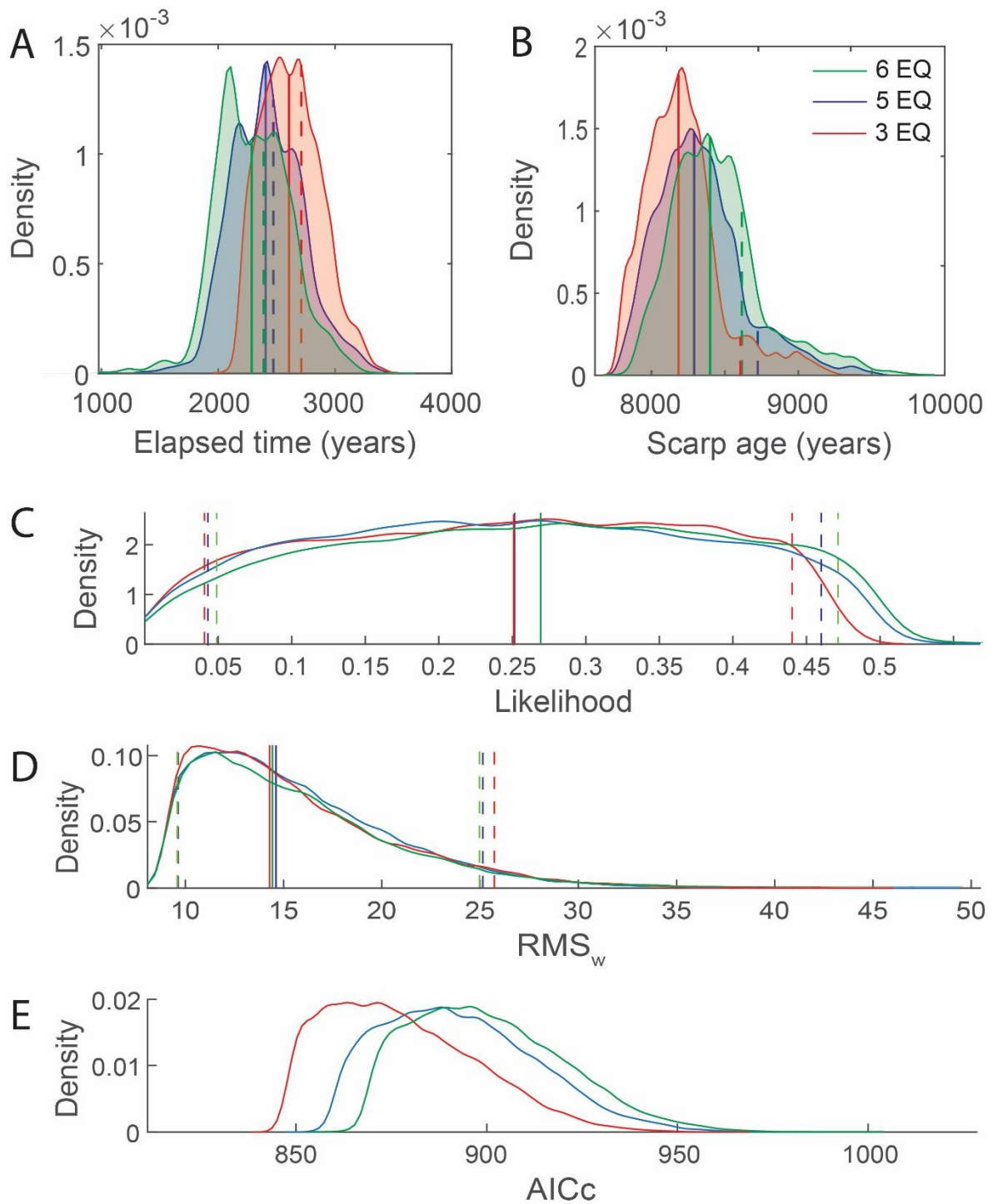
Fig. 4: Statistical plots for 160k Markov chain Monte Carlo (MCMC) model iterations, following removal of a 40k burn-in. Results are shown for three, five, and six model earthquakes. Vertical red lines indicate the median of each distribution, whereas vertical green lines indicate 95% confidence intervals. Posterior probability distribution functions from all models for A. Elapsed Time, and B. Scarp Age. Distributions of C. Likelihood, D. Weighted mean root square (RMS_w), and E. Corrected Akaike's Information Criterion (AICc) of slip history calculated for modelled ^{36}Cl concentrations compared to the measured values.
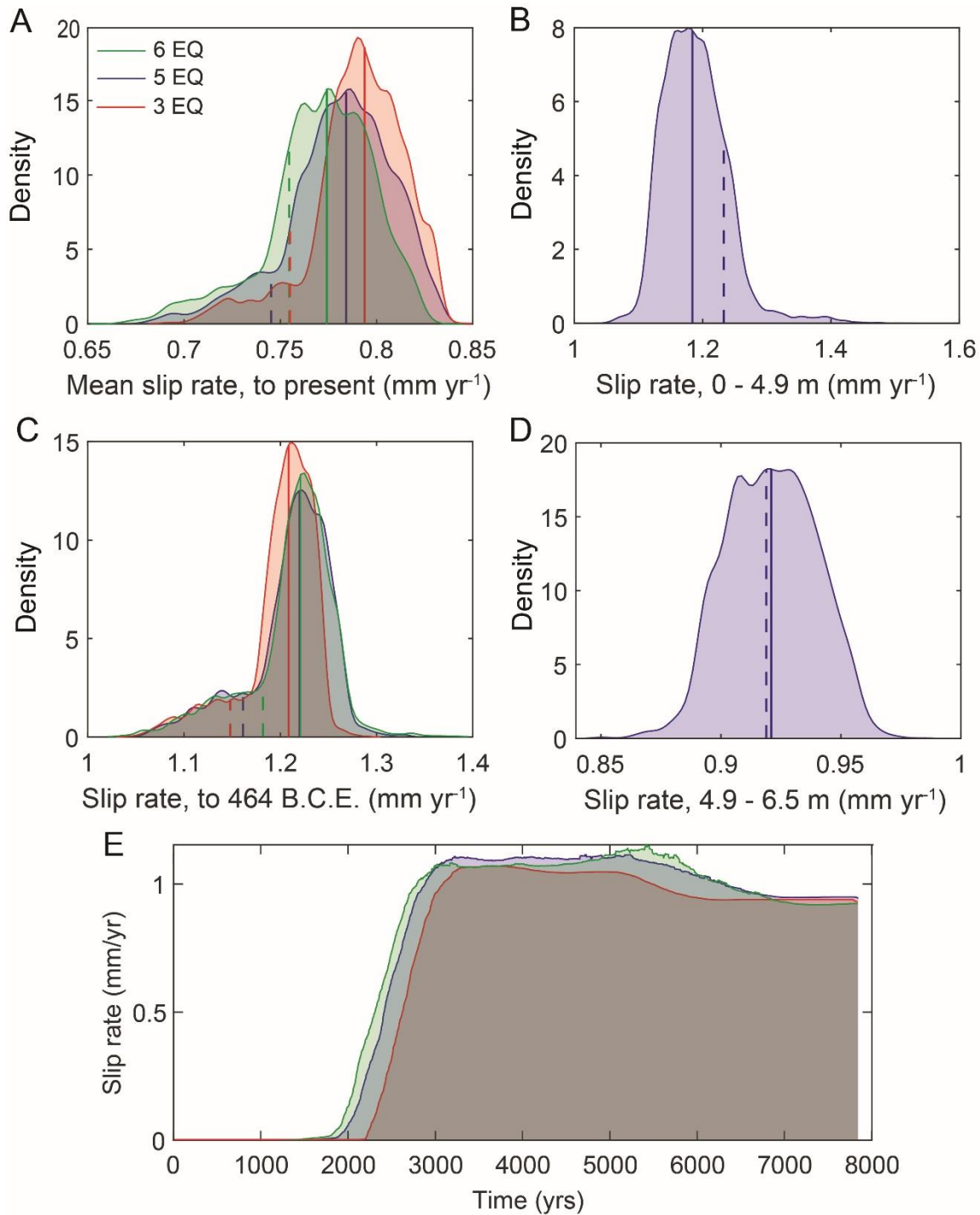
Fig. 5: Slip rates for the Sparta fault at Anogia (Anogia A plus drill core profile) from
Markov chain Monte Carlo modelling. Results are shown for three, five, and six model
earthquakes. In each panel, the most probable (top 10%) models calculated from the median
scarp age and scarp height are shown. Solid and dashed vertical lines indicate the mean and
maximum a posteriori probability (MAP) estimation for each distribution, respectively. Slip
rates are shown for three, five, and six model earthquakes, using a ^{36}Cl production rate of
59.4 ± 4.3 atoms g Ca^{-1} yr^{-1}. A. The distribution of the most probable slip rate for the entire
scarp calculated up to the present day. B. The distribution of the most probable slip rate for
the entire scarp calculated up to the last known earthquake at 464 B.C.E. C. The distribution

1090 of the most probable slip rate for lower segment of the scarp. D. The distribution of the most
1091 probable slip rate for the uppermost segment of the fault scarp. E. Mean slip rate over time.
1092 Slip rates using a ^{36}Cl production rate of 48.8 ± 3.5 atoms g Ca^{-1} yr^{-1} are shown in Fig. S2.

1093
1094
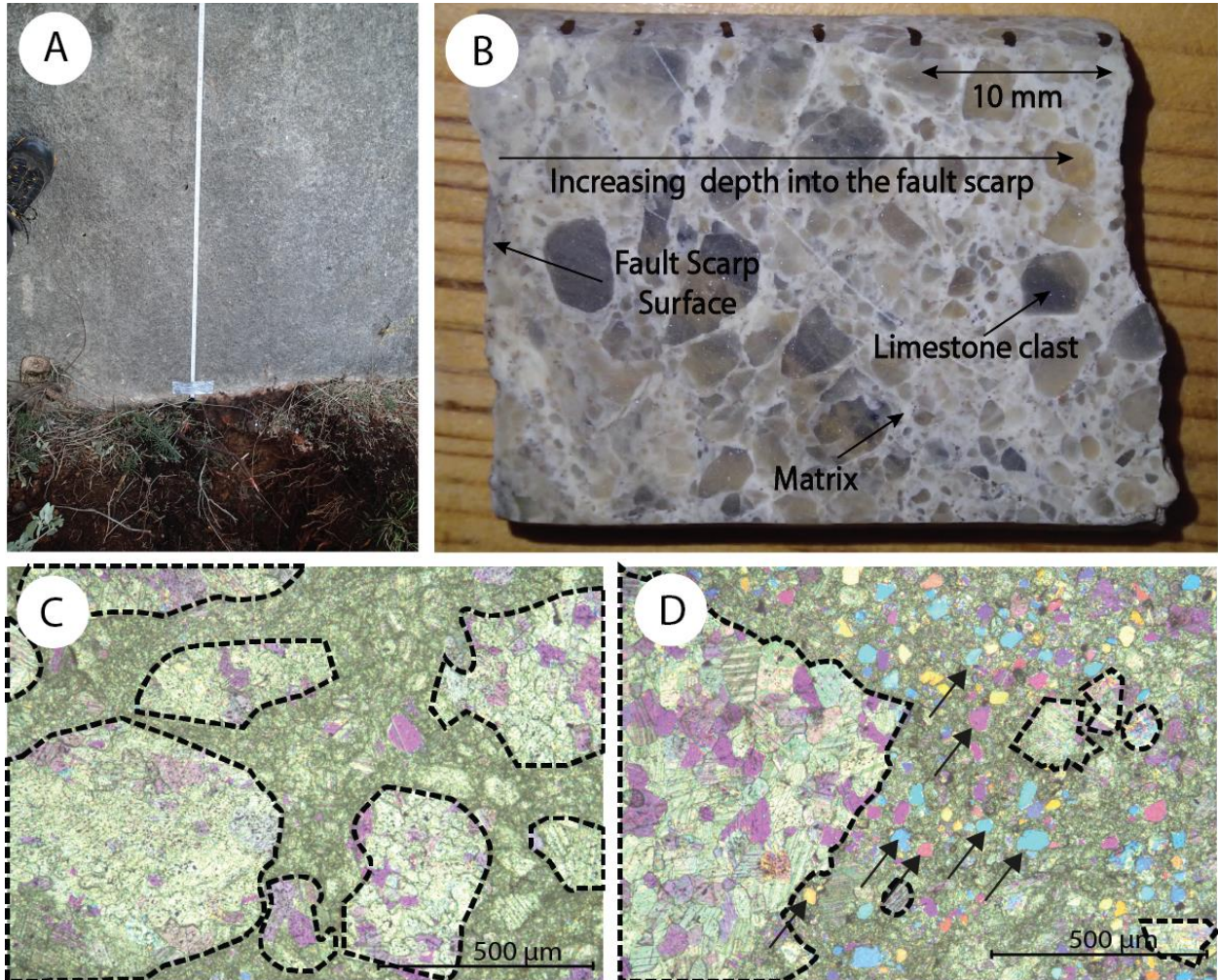
1095

1096 **Fig. 6:** The heterogeneous fault breccia that comprises the Sparta fault scarp surface. A. The
1097 Sparta fault scarp surface appears smooth and homogenous, as illustrated by this photograph
1098 of the scarp base at Anogia (upper half of the dug trench in the foreground). B. Fault breccia
1099 is revealed in a cut drill core, where clasts of host limestone are cemented in a fine matrix. C.
1100 A photomicrograph shows limestone clasts (dotted outlines) comprising about 60% of the
1101 thin section area. D. A photomicrograph shows fine matrix comprising about 60% of the thin
1102 section area. Arrows indicate quartz.

1103
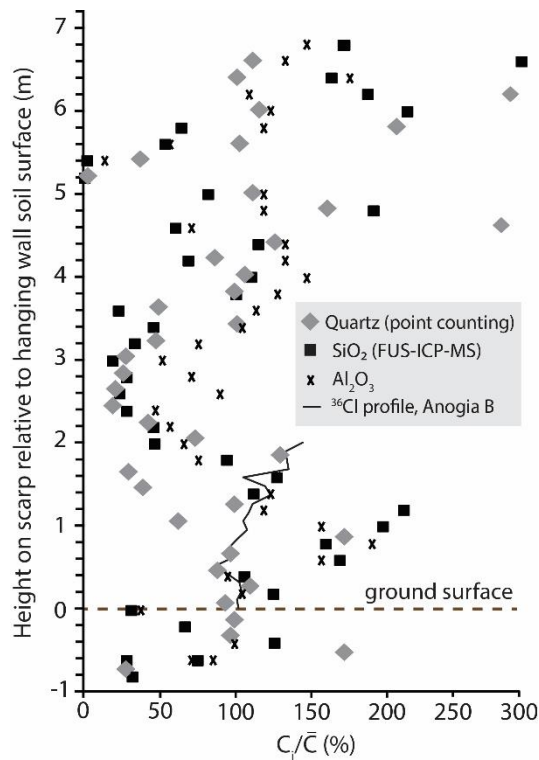
1104

Fig. 7: Concentrations of Al₂O₃ and SiO₂, and quartz abundances from point counting, along a vertical profile, Sparta fault scarp, Anogia. The concentration of each element (C_i) is normalized to its mean concentration through the profile ($C_i/\bar{C}$). The locations of former soil surface horizons inferred from ^{36}Cl concentrations and from the scarp geochemistry are shown for reference.
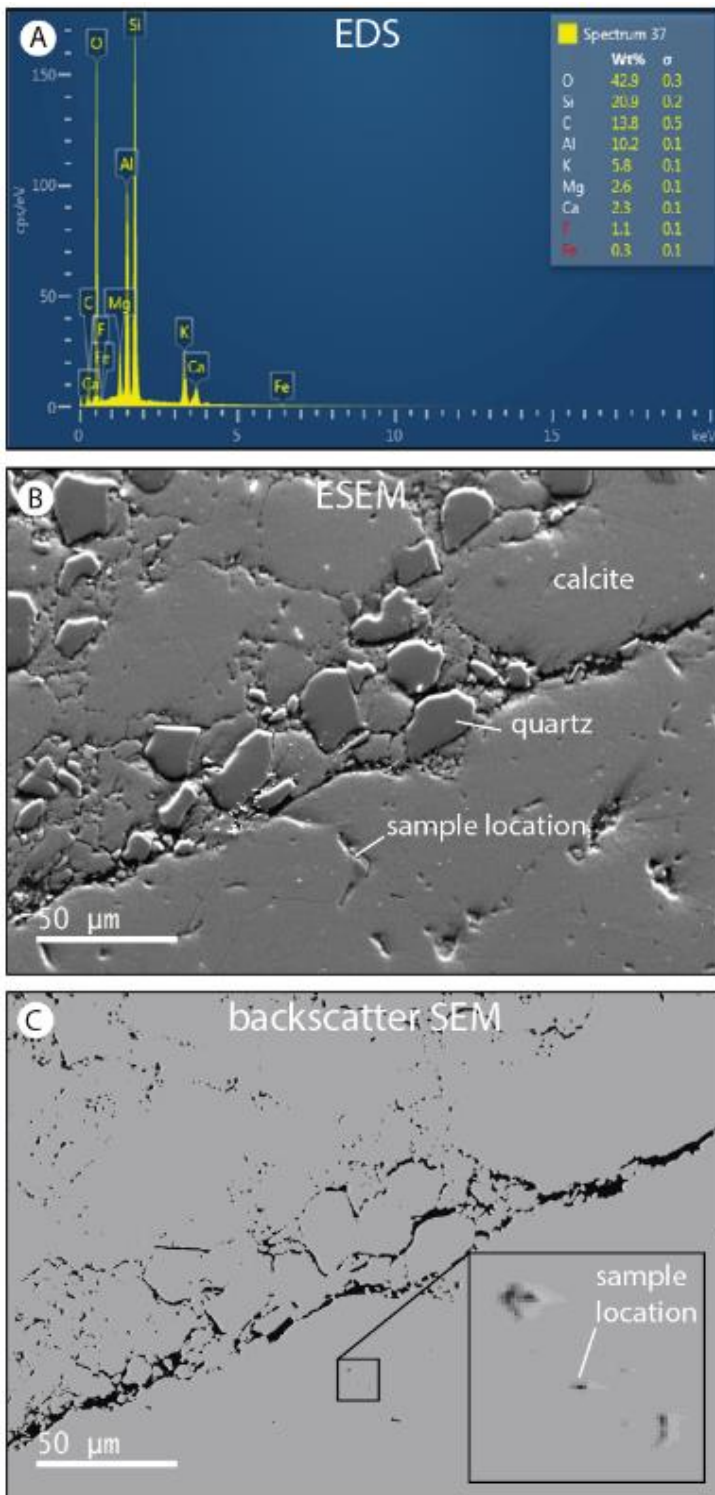
1110
1111 **Fig. 8:** Energy-dispersive X-ray spectroscope (EDS) elemental abundances, and
1112 environmental scanning electron microscope (ESEM) and backscatter SEM imagery of a thin
1113 section of fault breccia comprising the Sparta fault scarp surface at 1.1 m above the hanging
1114 wall. (A). Element abundances in a pore, the location of which is shown in panels B and C.
1115 Si, Al, and K are abundant relative to Ca, which indicates that clay, e.g., illite, is lining the
1116 pore. (B) Quartz is an abundant constituent of the thin section matrix. (C) Porosity, shown in
1117 black; note its spatial association with quartz. The location of the sample used in panel A is in
1118 a small pore, shown in the inset.

1119
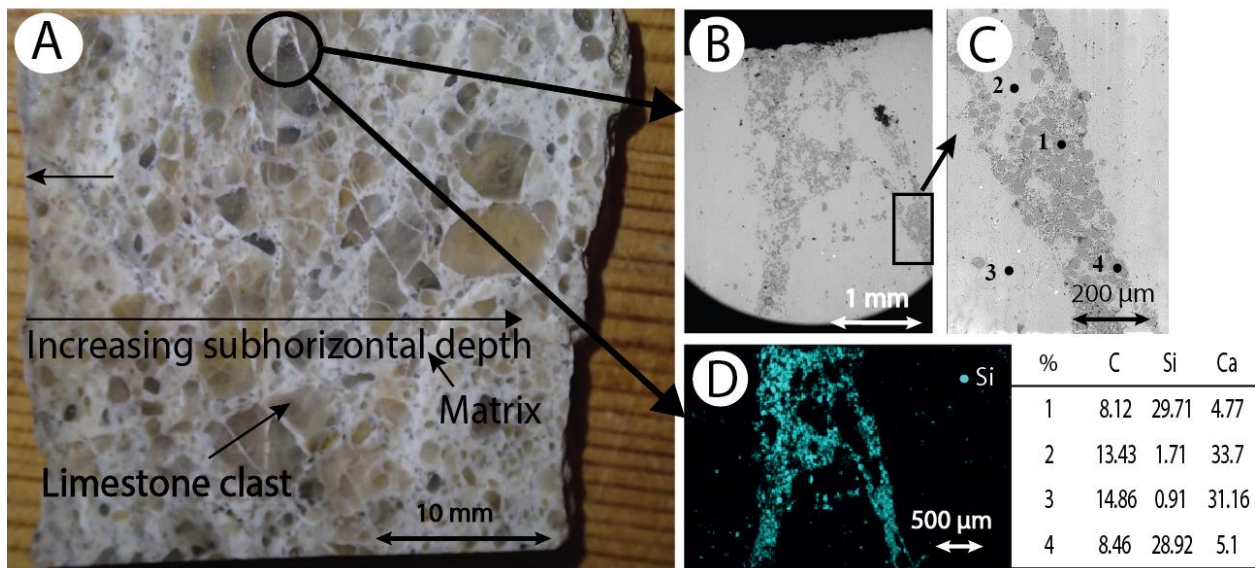
1120
1121 **Fig. 9:** Concentrations of Si in the Sparta fault breccia, 1.1 m above the scarp base at Anogia.
1122 A. A cut drill core from the Sparta fault scarp at Anogia showing limestone clasts cemented
1123 in fine matrix. The circled fine matrix is examined under high resolution in panels B to D. B.
1124 An ESEM image showing the sample location for spot elemental analysis (rectangle). C.
1125 Sample points for elemental analysis using EDS, with values shown in the table. D. The
1126 abundance of Si in the fine matrix illustrated in magenta for the circled part of the thin
1127 section shown in panel A.

1128

1129
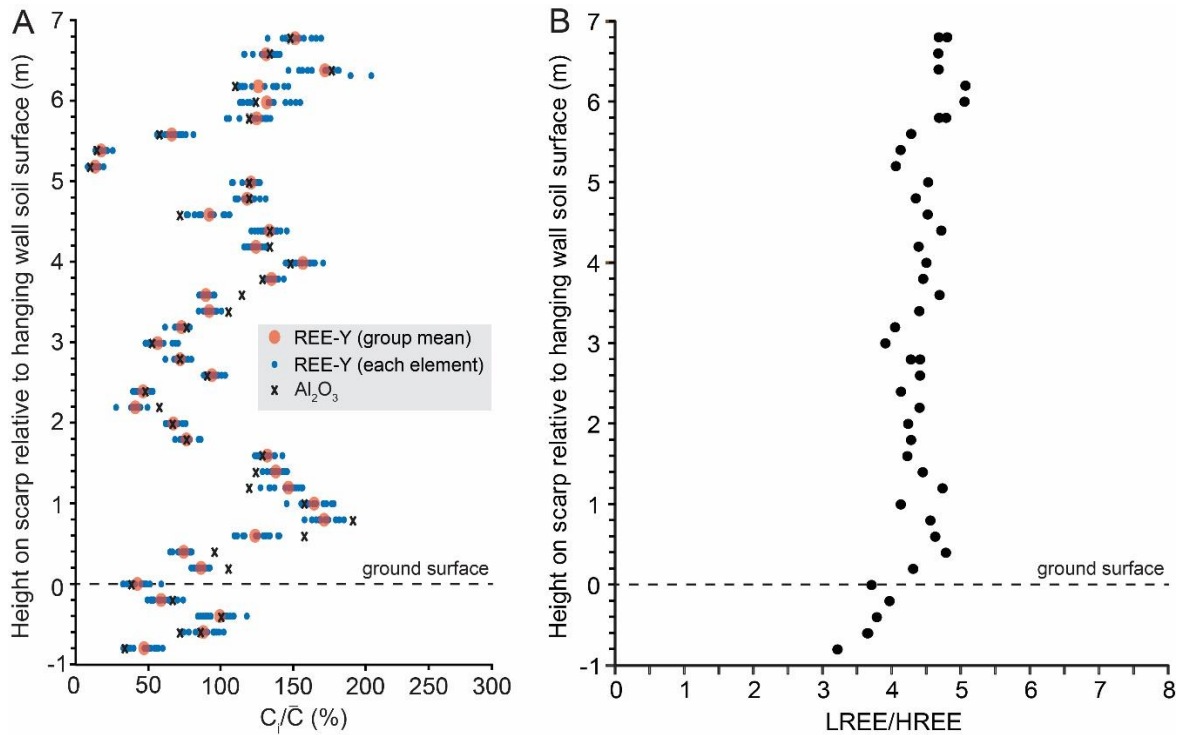
Fig. 10: Vertical distribution of REE-Y elements on the Sparta fault (Anogia B profile). A.
REE-Y concentrations. Mean values for all REE-Y elements at each sample point are shown
in red dots, whereas individual REE-Y elements are shown in blue dots. The concentration of
each element (C_i) is normalized to its mean concentration through the profile ($C_i/\overline{C}$).
Concentrations of Al_2O_3 and former soil surface horizons inferred from ^{36}Cl concentrations
profiles and geochemical data, are shown for reference. B. LREE:HREE ratio. There are two
measurements at -0.6 m.
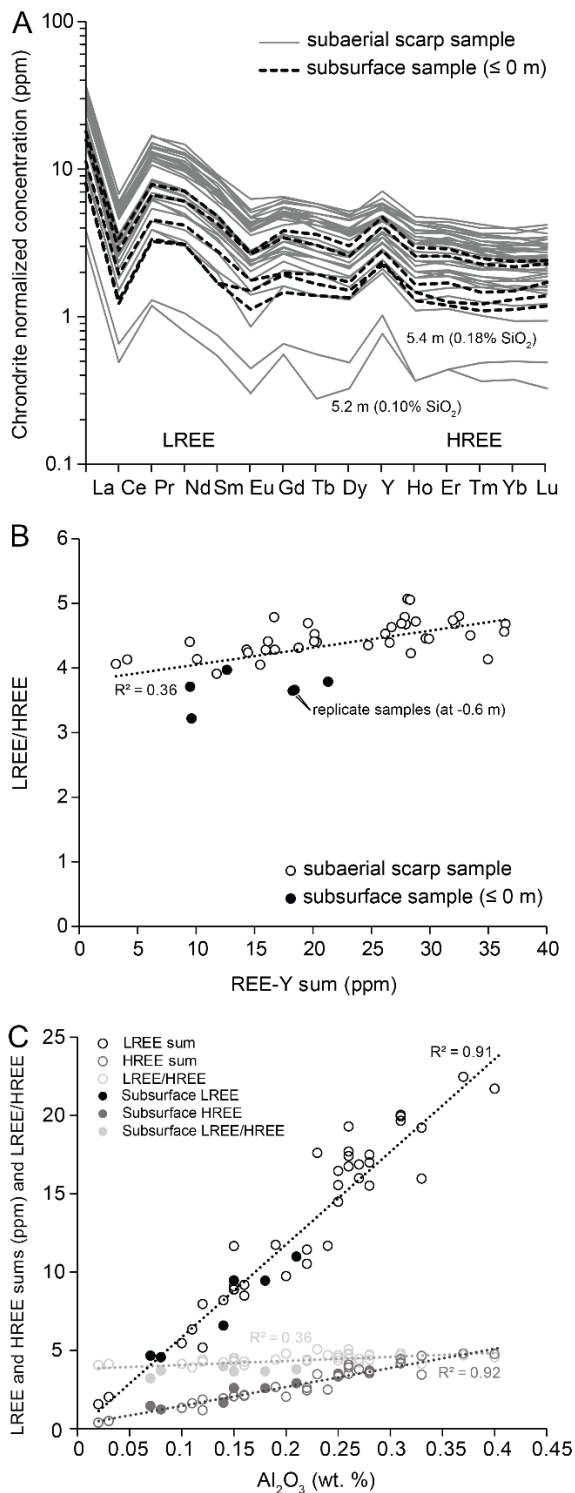
Fig. 11: REE-Y elements on the Sparta fault (Anogia B profile). A. Concentrations of rare-earth elements and yttrium (REE-Y) normalized to chondrite composition (McDonough and Sun, 1995). Each line shows a measured location on the scarp surface. The two low REE-Y outliers at 5.2 m and 5.4 m also have exceptionally low SiO_2 and Al_2O_3. B. LREE:HREE versus REE-Y sum. The R^2 value is for a linear fit. C. LREE, HREE, and LREE:HREE versus Al_2O_3 (wt.%). The R^2 values are for linear fits. In each panel, the six subsurface samples (≤ 0 m), including a replicate measurement at -0.6 m.

1151
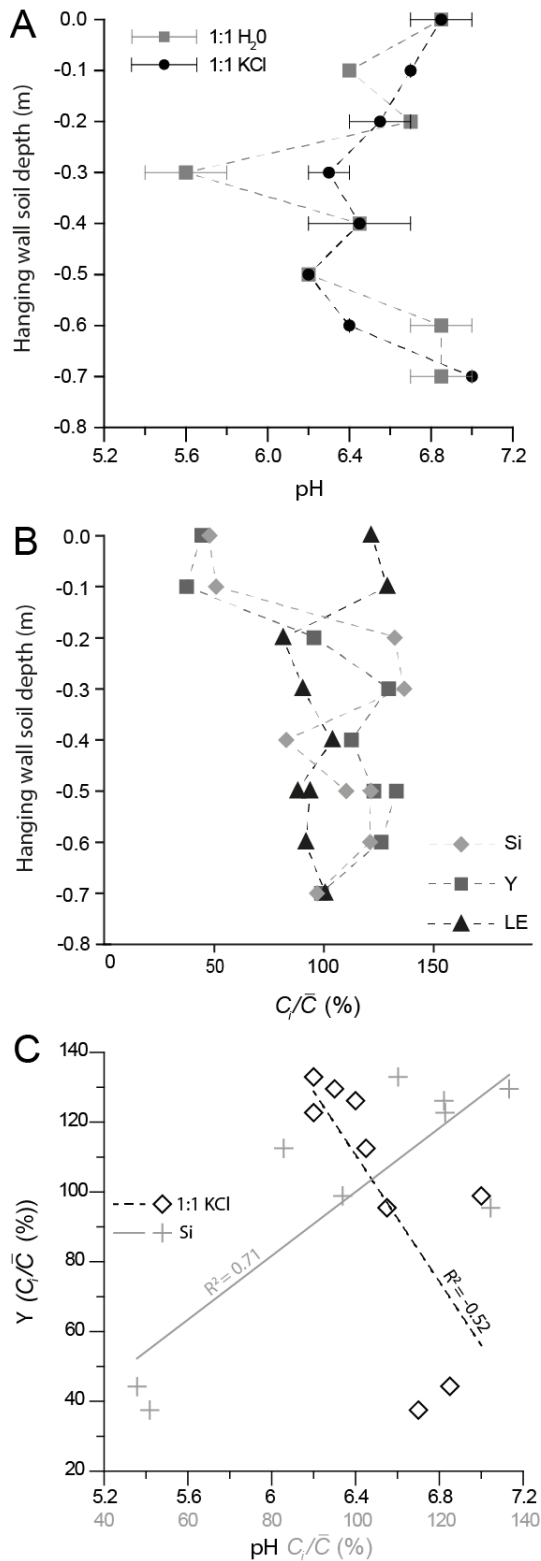
1152

Fig. 12: Hanging wall soil chemistry, adjacent to the Sparta fault scarp at Anogia. A. Soil pH
along a vertical profile measured from soil mixed with distilled H_2O and 1M KCl.
Uncertainty ranges show the ≤ 0.5 resolution of the indicator strips. B. Concentrations of Si,
Y, and elements too light to be measured using handheld XRF (LE, including C) along the
vertical soil profile. Each element has been normalized through division by its mean
concentration through the soil. C. Y concentrations plotted against pH (measured from 1:1
KCl) and Si concentration at each measured depth interval beneath the soil surface.